This is a preprint, the final version is subject to change, of the American Mineralogist (MSA)
Cite as Authors (Year) Title. American Mineralogist, in press.
(DOI will not work until issue is live.) DOI: http://dx.doi.org/10.2138/am-2017-6046
Revision 1

Carbocernaite from the Bear Lodge carbonatite, Wyoming: revised structure, zoning and rare-earth fractionation on a microscale

Anton R. Chakhmouradian [a,]*, Mark A. Cooper [a], Ekaterina P. Reguir [a], and Meghan A. Moore [b]

[a] *Department of Geological Sciences, University of Manitoba, Winnipeg, Manitoba, Canada*

[b] *4016 West Lennox Loop, Coeur d'Alene, Idaho, USA*

* Corresponding author at: 125 Dysart Road, Department of Geological Sciences, University of Manitoba, Winnipeg, Manitoba, R3T 2N2, Canada. Tel.: +1 204 474 7278; fax: +1 204 474 7623. E-mail address: Anton.Chakhmouradian@umanitoba.ca.

ABSTRACT

Zoned crystals of carbocernaite occur in hydrothermally reworked burbankite-fluorapatite-bearing calcite carbonatite at Bear Lodge, Wyoming. The mineral is paragenetically associated with pyrite, strontianite, barite, ancylite-(Ce) and late-stage calcite, and is interpreted to have precipitated from sulfate-bearing fluids derived from an external source and enriched in Na, Ca, Sr, Ba and rare-earth elements (REE) through dissolution of the primary calcite and burbankite. The crystals of carbocernaite show a complex juxtaposition of core-rim, sectoral and oscillatory zoning patterns arising from significant variations in the content of all major cations, which can be expressed by the empirical formula $(Ca_{0.43\text{-}0.91}Sr_{0.40\text{-}0.69}REE_{0.18\text{-}0.59}Na_{0.18\text{-}0.53}Ba_{0\text{-}0.08})_{\Sigma 1.96\text{-}2.00}(CO_3)_2$. Interelement correlations indicate that the examined crystals can be viewed as a solid solution between two hypothetical end-members, $CaSr(CO_3)_2$ and $NaREE(CO_3)_2$, with the most Na-REE-rich areas in pyramidal (morphologically speaking) growth sectors representing a probable new mineral species. Although the Bear Lodge carbocernaite is consistently enriched in light REE relative to heavy REE and Y (chondrite-normalized La/Er = 500-4200), the pyramidal sectors exhibit a greater degree of fractionation between these two groups of elements

relative to their associated prismatic sectors. A sample approaching the solid solution midline [$(Ca_{0.57}Na_{0.42})_{\Sigma 0.99}(Sr_{0.50}REE_{0.47}Ba_{0.01})_{\Sigma 0.98}(CO_3)_2$] was studied by single-crystal X-ray diffraction and shown to have a monoclinic symmetry [space group *P*11*m*, *a* = 6.434(4), *b* = 7.266(5), *c* = 5.220(3) Å, γ = 89.979(17)°, *Z* = 2] as opposed to the orthorhombic symmetry (space group $Pb2_1m$) proposed in earlier studies. The symmetry reduction is due to partial cation order in sevenfold-coordinated sites occupied predominantly by Ca and Na, and in tenfold-coordinated sites hosting Sr, REE and Ba. The ordering also causes splitting of carbonate vibrational modes at 690-740 and 1080-1100 cm^{-1} in Raman spectra. Using Raman micro-spectroscopy, carbocernaite can be readily distinguished from burbankite- and ancylite-group carbonates characterized by similar energy-dispersive spectra.

INTRODUCTION

Carbocernaite was discovered by Bulakh et al. (1961) in dolomite-calcite carbonatites and calcite veins at the Vuoriyarvi intrusive complex in northern Karelia, Russia. The name was chosen to reflect the presence of carbonate groups, cerium and sodium (Na) in its composition, which was initially given as $(Ca,Na,REE,Sr,Ba)CO_3$ (REE = rare-earth elements). Subsequently, this mineral was reported also from carbonatites at Weishan (China), Phan Si Pan (Vietnam), Khanneshin (Afganistan), Sarnu-Dandali, Newania, Khamambettu, Kamthai (India), Swartbooisdrif, Kalkfeld and Ondurakorume (Namibia), Araxá and Jacupiranga (Brazil), Rocky Boy (Montana, USA), Sturgeon Narrows (Canada), Korsnäs (Finland), Khibiny, Ozerny and Biraya in Russia (Bulakh and Izokh 1967; Harris 1972; Eremenko and Vel'ko 1982; Wall et al. 1993; Zhang et al. 1995; Reguir and Mitchell 2000; Traversa et al. 2001; Orris and Grauch 2002; Pekov and Podlesnyi 2004; Wall and Zaitsev 2004; Drüppel et al. 2005; Coztanzo et al. 2006; Doroshkevich et al. 2010; Mills et al. 2012; Bhushan and Kumar 2013; Burtseva et al. 2013). In addition, carbocernaite was described from metasomatized REE-rich dolomite in the West mine of the Bayan Obo deposit, China (Zhang et al. 1995) and from miarolitic cavities in alkaline igneous rocks at Mont Saint-

Hilaire, Canada (Horváth and Gault 1990) and Khibiny, Russia (Pekov and Podlesnyi 2004). Notably, over one-half of these reports are not backed by any convincing analytical evidence. For example, Harris (1972), Traversa et al. (2001), and Bhushan and Kumar (2013) did not record any Na in their samples, which calls into question the validity of these identifications.

The current understanding of the crystal structure of carbocernaite is also inadequate. The structure was first determined by Voronkov and Pyatenko (1967), who used for this purpose a sample of unknown composition from an unspecified locality, although definitely not the type material of Bulakh et al. (1961). Voronkov and Pyatenko (1967) identified the symmetry as orthorhombic (space group $Pb2_1m$), and recognized the presence of two symmetrically non-equivalent cation sites in the structure (*A* and *B*) coordinated by seven and ten oxygen atoms, respectively, and arrived at the following structural formula based on the average composition calculated from published data: $(Na,Ca)(REE,Sr,Ca,Ba)(CO_3)_2$. Shi et al. (1982) examined the chemistry and structure of the Bayan Obo material and refined the formula to $(Ca,Na)(Sr,REE,Ba)(CO_3)_2$; according to these authors, the larger cation site dominated by Sr is coordinated by eight oxygen atoms, and not ten as in the earlier refinement. Neither Voronkov and Pyatenko (1967) nor Shi et al. (1982) reported the final agreement factors for their refinements.

The confirmed occurrences of carbocernaite in carbonatites are diverse in form and include: (1) discrete crystals and clusters (Bulakh et al. 1961); (2) exsolution lamellae in primary calcite (Wall et al. 1993); (3) pseudomorphs after primary burbankite (Wall and Zaitsev 2004); (4) pseudomorphs after calcite or ankerite (Drüppel et al. 2005); and (5) overgrowths on cordylite-(La) (Biraya: P.M. Kartashov, pers. commun.). It is noteworthy that, in the absence of X-ray diffraction and quantitative chemical data, the identification of carbocernaite is not trivial because it is optically similar (strongly birefringent, biaxial negative) to members of the calcioancylite-(Ce) – ancylite-(Ce) series, $(Ca,Sr)_{2-x}REE_x(CO_3)_2(OH)_x \cdot (2-x)H_2O$ (Dal Negro et al. 1975). Although ancylite-group minerals lack detectable Na, the low-intensity Na peak in energy-dispersive spectra of some carbocernaite is easy to overlook during routine examination

of samples. It is thus very likely that (a) this mineral is significantly more common in carbonatites than the relatively few confirmed localities known to date, and (b) ancylite-group minerals at some localities may have been misidentified as carbocernaite (see above). Raman micro-spectroscopy, which is an inexpensive "fingerprinting" technique that can be used effectively for fast identification of carbonates with a spatial resolution of ~1 μm (Herman et al. 1987), has not been applied to discriminating between carbocernaite and compositionally similar minerals yet because their spectra are not available.

In the present work, we identified carbocernaite as part of REE mineralization in carbonatites at Bear Lodge, Crook Co., northeastern Wyoming, USA (Moore et al. 2015; Ray and Clark 2015). One of the samples proved particularly interesting because it contained zoned crystals representing a wide range of carbocernaite compositions and in quantity sufficient for their detailed examination by a variety of instrumental techniques. Our primary objectives were to attain a better understanding of the crystal chemistry of carbocernaite, its structural relations with other anhydrous carbonate phases, and also to provide spectroscopic data to enable reliable identification of this mineral in micron-sized samples.

OCCURRENCE AND PARAGENESIS

From 2004 to 2013, the Bear Lodge alkaline intrusive complex (ca. Lat. 44°30′ N, Long. 104°26′ W) was actively explored by Rare Element Resources as a potential source of rare earths (Noble et al. 2013). Much of the company's exploration efforts focused on the Bull Hill diatreme in the central part of the complex, where numerous carbonatite dikes intersect heterolithic intrusive breccias of largely phonolitic composition. The geology of the complex has been addressed in sufficient detail elsewhere (Staatz 1983; Noble et al. 2009; Moore et al. 2015; Ray and Clark 2015) and will not be repeated here. The material studied in the present work was sampled from hole RES08-4 drilled by Rare Element Resources in the Bull Hill Southwest target area. The available whole-rock trace-element, radiogenic and stable-isotopic

data (Table 1) are indicative of a carbonated subcontinental lithospheric source modified by subduction (for detailed discussion, see Moore et al. 2015).

In terms of the paragenetic classification of Moore et al. (2015), the sample studied in the present work can be attributed to the early-crystallizing burbankite paragenesis. It is a cavernous medium-grained rock composed predominantly of primary calcite (Table 1), marcasite overgrown by pyrite (~30 vol.% of the rock), minute subhedral grains of fluorapatite and galena, xenocrystic potassium feldspar, scarce hexagonal prismatic crystals of burbankite showing evidence of incipient resorption (Fig. 1a), and much more abundant cavernous pseudomorphs after burbankite (~6 vol.%). Large pseudomorphs contain both relict burbankite and products of its alteration [ancylite-(Ce), strontianite, barite and calcite]; smaller ones comprise only sub- to euhedral crystals of the secondary phases (Fig. 1b). In addition to this late-stage mineralization confined to the pseudomorphs, the sample also contains irregularly shaped dissolution cavities lined with pyrite cubes, calcite rhombohedra, and prismatic carbocernaite crystals of pale yellow color up to 2 mm in length, which are the subject of this report. Some of the cavities also contain small rhombohedral crystals of late-stage calcite, long-prismatic to subhedral grains of zoned Ca- Ba-rich strontianite (1.5-9.5 wt.% CaO; 0.9-4.2 wt.% BaO) and anhedral barite developed interstitially with respect to the carbocernaite (Figs. 1c, 1d). The latter mineral is locally replaced by ancylite-(Ce) developing both along fractures and as euhedral overgrowths (Fig. 1e). The order of crystallization is: pyrite, carbocernaite, strontianite, barite + ancylite-(Ce), calcite. The primary calcite shows a discontinuous rim depleted in Sr along grain boundaries and around dissolution cavities (Fig. 1f). In contrast to the primary calcite (0.5-0.8 wt.% FeO, 4.5-5.4 wt.% MnO, 0.7-0.8 wt.% SrO, < 0.05 wt.% BaO), the late-stage variety is depleted in Fe and Mn, but enriched in Sr and Ba (< 0.1, 0.4-1.6, 0.8-1.8 and 0.3-1.0 wt.% respective oxides). The two varieties are similar in C isotopic composition, but differ strongly in $\delta^{18}O_{V\text{-}SMOW}$ value (Table 1). Pyrite crystals lining cavities are depleted in heavy S ($\delta^{34}S_{V\text{-}}$

$_{CDT} \approx -9.3‰$), particularly in comparison with pyrite from other carbonatites, including those affected by orthomagmatic hydrothermal activity ($\delta^{34}S_{V\text{-}CDT} = -2.4 - +5.1‰$: Drüppel et al. 2006; Farrell et al. 2010).

ZONING AND COMPOSITIONAL VARIATION

Methodology

Several carbocernaite crystals were extracted from a vug, mounted in epoxy and analyzed using microbeam techniques. Back-scattered electron (BSE) images were used for the selection of areas suitable for quantitative analysis. The concentrations of major and some minor elements were determined by wavelength-dispersive spectrometry (WDS) using a Cameca SX 100 automated electron microprobe operated at 15 kV and 20 nA. The electron beam was defocused to 10 μm to minimize Na loss. The following natural and synthetic standards were employed in the analysis: albite (Na), fluorapatite (Ca), fayalite (Fe), $SrTiO_3$ (Sr), $Ba_2NaNb_5O_{15}$ (Ba), REE orthophosphates (Y, La, Ce, Pr, Nd, Sm) and ThO_2 (Th). Iron was found not to be present at detectable levels (> 700 ppm) in any of the samples.

The abundances of selected trace elements were measured by laser-ablation inductively-coupled-plasma mass-spectrometry (LA-ICPMS) using a 213-nm Nd-YAG Merchantek laser connected to a Thermo Finnigan Element 2 sector-field instrument. The data were collected using spot analysis with a 30 μm laser beam at a repetition rate of 5-10 Hz and power level of 80-85%. The incident pulse energy was 0.03-0.07 mJ, yielding a surface energy-density of 4.0-5.6 J/cm^2. The ablation was performed in Ar (plasma and auxiliary) and He (sample) atmospheres. The rate of oxide production was monitored during instrument tuning by measuring the ThO/Th ratio and kept below 0.2%. Synthetic glass standard NIST SRM 610 (Norman et al. 1996) was employed for calibration and quality control. After taking into account potential spectral overlaps and molecular interferences, the following isotopes were chosen for analysis: ^{55}Mn, ^{85}Rb, ^{89}Y, ^{137}Ba, ^{139}La, ^{140}Ce, ^{141}Pr, ^{143}Nd, ^{147}Sm, ^{151}Eu, ^{155}Gd, ^{159}Tb, ^{163}Dy, ^{165}Ho, ^{167}Er, ^{169}Tm, ^{172}Yb, ^{175}Lu, ^{208}Pb, ^{232}Th and ^{238}U. The Ce contents determined by WDS served as an internal standard. All

142 analyses were performed in a low-resolution mode (~300) using Pt skimmer and sample cones. Data
143 reduction was carried out online using the GLITTER software (van Achterbergh et al. 2001) and an in-
144 house Excel-based program. Quality control was ensured by keeping the fractionation at less than 10%
145 and fractionation/error ratio at less than three. Rubidium was found not to be present at detectable
146 levels (> 10 ppm) in any of the samples.
147
148 *Results*
149 The crystals of carbocernaite are optically uniform in transmitted light, but exhibit strong sector
150 zoning in back-scattered electron (BSE) images (Fig. 2). Their central part (referred to hereafter as the
151 core) is irregularly shaped and characterized by a fairly uniform, low average atomic number (AZ). From
152 the core outward, two types of sectors can be identified: medium-AZ prismatic and high-AZ pyramidal.
153 Note that these terms are used strictly in a morphological sense (as one would refer to a crystal habit,
154 for example), and have no crystallographic connotations. The sectors are separated by an undulating
155 suture, indicating fluctuations in the relative growth rates of prism and pyramid faces. Finer-scale
156 oscillatory zoning is superposed on the sector pattern, but is more prominent in the high-AZ sectors; the
157 width of individual zones ranges from a few μm to 100 μm.
158 The observed variations in AZ reflect changes in the content of Na, Ca, Sr, Ba and REE between and
159 across individual sectors (Tables 2, 3). As shown in Figures 3a-c, the core is consistently enriched in Ca,
160 Sr and Ba (15.0-20.5, 25.0-28.6 and 1.5-4.5 wt.% respective oxides), but poor in Na and light REE (2.4-3.6
161 and 12.6-18.8 wt.% respective oxides) relative to the prismatic and pyramidal sectors. The latter exhibit
162 the highest Na and REE (up to 6 wt.% Na_2O and 35 wt.% $LREE_2O_3$), but the lowest Ca and Sr levels (9.6
163 and 15.5 wt.% respective oxides) recorded not only in the Bear Lodge samples, but also among all
164 carbocernaite compositions reported to date. The medium-AZ prismatic sectors are generally higher in
165 Ca and Sr, but lower in Na and LREE, relative to the pyramidal sectors; however, both show an

appreciable variation in the content of all major elements so that their compositional ranges overlap (for example, cf. analyses 2-4 in Table 2, or D and G in Table 3). The overall compositional range of the Bear Lodge carbocernaite can be expressed with the following formula, calculated on the basis of two carbonate groups: $(Ca_{0.43-0.91}Sr_{0.40-0.69}LREE_{0.18-0.59}Na_{0.18-0.53}Ba_{0-0.08})_{\Sigma 1.96-2.00}(CO_3)_2$. The small deficit (≤ 2%) of large cations is within the analytical uncertainty, although the presence of vacancies in the structure cannot be ruled out. Published compositions give cation totals as low as 1.93 (Bayan Obo: Zhang et al. 1995), and significant proportions of vacancies have been reported in other Na-Ca-Sr-REE carbonates (Onac et al. 2009 and references therein). The majority of carbocernaite compositions from this work and the literature can be approximated as a solid solution among $CaSr(CO_3)_2$, $NaCe(CO_3)_2$ and $CaBa(CO_3)_2$. In most cases, the first two hypothetical end-members contribute > 90 mol.%, but one sample from Vuoriyarvi (Wall and Zaitsev 2004, their Table 10.3) has $CaBa(CO_3)_2 > NaCe(CO_3)_2$.

In terms of trace-element variations (Table 3), Mn is lowest in the core (40-65 ppm) and highest in the prismatic sectors (130-290 ppm), whereas the pyramidal zones show intermediate levels of this element (52-104 ppm). The distribution of REE is more complex and serves as a convincing illustration of intersectoral variations in the crystal-fluid partitioning of these elements. All three compositionally distinct domains show the strong predominance of LREE over heavy REE (HREE), but the relative degree of light lanthanide enrichment varies significantly across the crystal. Because HREE beyond Er were not detectable in the core, we used the chondrite-normalized La/Er ratio as a proxy to LREE/HREE fractionation. The Sr/Na ratio is highest in the core and lowest in the pyramidal sectors, and thus was chosen to correlate the measured $(La/Er)_{cn}$ values to a specific zone. As can be seen from Figure 3d, the core has $(La/Er)_{cn}$ values transitional between those in the medium-AZ (prismatic) and high-AZ (pyramidal) zones. The degree of LREE/HREE fractionation is greater in the latter, so much so in fact that they show higher levels of LREE, but *lower* concentrations of heavy lanthanides and Y in comparison with the prismatic sectors (cf., for example, analyses C and G in Table 3). It appears that with increasing

Na and REE contents (i.e. decreasing Sr/Na ratio in Fig. 3d), carbocernaite shows a tendency for crystallographically controlled uptake of REE, which involves preferential incorporation of larger lanthanides into the pyramidal growth sectors at Sr/Na < 10. As can be expected, the chondrite-normalized REE profiles of the two types of sectors differ in slope (Fig. 3e). To our knowledge, this is only a third documented example of intersectoral LREE/HREE fractionation in minerals (cf. Cressey et al. 1999; Baele et al. 2012). Remarkably, the examined crystals show little variation in REE ratios sensitive to changes in redox regime {$\delta Ce = Ce_{cn}/[0.5 \times (La_{cn} + Pr_{cn})]$; $\delta Eu = Eu_{cn}/[0.5 \times (Sm_{cn} + Gd_{cn})]$}, or in ligand chemistry (Y/Ho) (Chakhmouradian and Wall 2012). All three values are consistently subchondritic: $\delta Ce = 0.77 \pm 0.05$, $\delta Eu = 0.78 \pm 0.08$ and $Y/Ho = 21 \pm 3$ (based on 31 LA-ICPMS measurements). Substituents other than Mn and REE do not show any consistent variation among the zones.

SINGLE-CRYSTAL X-RAY DIFFRACTION

Data collection

A $40 \times 80 \times 80$ μm grain was extracted from the area in a polished mount whose composition approaches the midline in the $CaSr(CO_3)_2 – NaCe(CO_3)_2$ solid solution (see Fig. 2b for sample location). The grain was attached to a tapered glass fiber, and mounted on a Bruker D8 three-circle diffractometer equipped with a rotating-anode generator (Mo*K*α X-radiation), multi-layer optics and an APEX-II detector. A total of 9331 intensities was collected to 60° 2θ using 12 s per 0.3° frame with a crystal-to-detector distance of 5 cm. Empirical absorption corrections (SADABS: Sheldrick, 2008) were applied and identical reflections were merged, resulting in 2870 reflections within the Ewald sphere. The structure was initially refined in $Pb2_1m$ using the starting coordinates of Voronkov and Pyatenko (1967). However, there were numerous reflections observed (with intensities up to 20 sigma level!) of the type 0*kl* with *k* = odd, which violate both the *b*-glide and 2_1 screw axis. A 0*kl* precession-geometry slice was constructed from the entire frame series, and the violating reflections can be clearly identified (Fig. 4). As an ordered

cation distribution may be responsible for the detected symmetry reduction, the $Pb2_1m$ structure model was expanded to $P1$ symmetry to test for this possibility. In $P1$ symmetry, the large cation sites each split into two non-equivalent sites. Refined site-occupancies gave significantly different scattering values for the two sevenfold-coordinated and two tenfold-coordinated sites, in support of partial cation ordering, resulting in lower symmetry. The $P1$ model contained a mirror plane perpendicular to [001], and we adopted the monoclinic space group Pm with the **c** axis unique ($P11m$), so as to maintain the original axial setting of Voronkov and Pyatenko (1967). A slight improvement was seen for the merging of equivalent reflections in $P11m$ (R_{merge} = 1.0% for 1588 unique), as compared to $Pb2_1m$ (R_{merge} = 1.9% for 859 unique), again in support of the underlying lower monoclinic symmetry. A fully anisotropic structural model in $P11m$, incorporating variable refining site-scattering for the large cation sites gave an R value of 3.1% (Table 4). The possibility of twinning is always present in space groups with strong pseudosymmetry, and a refining twin (1 0 0 / 0 -1 0 / 0 0 -1) in combination with racemic twinning (-1 0 0 / 0 -1 0 / 0 0 -1) was added (i.e. twofold rotation about the **a** axis and the addition of a centre of symmetry), reducing the final R value to 1.6%. The unit cell parameters are based on a least-squares refinement of 4085 reflections with ($I > 10\sigma I$).

Structure refinement

The $P11m$ structural model contains the same site labels used by Voronkov and Pyatenko (1967), as well as a similarly named set of sites marked with a prime, which are approximately related to the first set of coordinates by the operation ($-x$, $y + ½$, z). In the monoclinic model, the sites positioned on the mirror (z = 0, ½) have no equivalent, and the sites positioned off the mirror are related by a symmetry-equivalent site at x, y, $-z$. The site-fractional coordinates are given in Table 5, and the pseudosymmetric site-pairings related by ($-x$, $y + ½$, z) are compared in Table 6. In regards to the final refined atom positions, the most significant departure from $Pb2_1m$ symmetry is evidenced in the refined x coordinate

value for the *A*, *A*' and *B*, *B*' sites and for the *y* coordinate value for the O3, O3' sites. In agreement with the findings of Voronkov and Pyatenko (1967), our *A*, *A*' sites are dominantly occupied by Ca and Na, and the *B*, *B*' sites by Sr, Ba and the lanthanides. We allowed for variable refining site-scattering at the *A*, *A*' sites with assigned Ca and Na scattering factors, and at the *B*, *B*' sites with assigned Ce and Sr scattering factors, in accord with the WDS analysis (Table 2, analysis 5): $(Ca_{0.569}Na_{0.420}Sr_{0.502}La_{0.147}Ce_{0.234}Pr_{0.023}Nd_{0.056}Sm_{0.009}Ba_{0.013}Th_{0.001})_{\Sigma 1.974}(CO_3)_2]$. This gave the following site-scattering values (in electrons per formula unit, epfu): 8.1(1) at *A*, 8.5(1) at *A*', 21.6(1) at *B*, and 23.9(1) at *B*'. The largest departure in refined site-scattering values supporting the lower *P*11*m* symmetry, is between *B* and *B*' (~10% relative difference), where the two epfu values differ from each other by > 20 times the standard error. The individual and mean bond-lengths are given in Table 7, and minor differences can be identified between the *A*, *A*' and *B*, *B*' polyhedra. It is tempting to try and assign the elements in a quantitative manner between the *A*, *A*' and *B*, *B*' sites to better understand any partial cation-ordering differences; however, any specific site-assignment result is somewhat lacking in certainty (see below).

The *A*, *A*' sites that are coordinated by seven anions are presumed to contain the Ca and Na from the chemical analysis, and this is in good accord with the observed site-scattering at these sites and the observed mean bond-lengths. The refined site-scattering at the *A*' site is slightly greater than for the *A* site, and the <*A*' – O> bond length is slightly shorter than the <*A* – O> bond length; if only Ca and Na resided at these two sites, this would suggest that the *A*' site contains slightly more Ca relative to the Ca content at *A* (as Ca and Na in a sevenfold coordination have a radius of 1.06 and 1.12 Å, respectively; Shannon 1976). However, the measured Ca+Na content of 0.99 (i.e. slightly less than the ideal value) indicates that a third cation may also be present at the *A*, *A*' sites. Of the remaining cations (all with appreciably greater scattering than Ca and Na), we cannot establish with any certainty which one may reside at *A* or *A*'. Therefore, within a reasonable margin of error, a single reliable site assignment

solution is not possible for the *A*, *A*' sites. For the *B*, *B*' sites, which involve more occupants, individual site assignments would be even less reliable. We have therefore elected to group the *A*, *A*' and *B*, *B*' sites together and refer to them collectively as *A** and *B** (with each contributing 1 apfu). The total observed site-scattering at *A** is 16.6 epfu, and the $Ca_{0.57}Na_{0.42}$ from the WDS data gives 16.0 epfu. The total observed site-scattering at *B** is 45.5 epfu, and the $Sr_{0.50}La_{0.15}Ce_{0.23}Pr_{0.02}Nd_{0.06}Sm_{0.01}Ba_{0.01}$ from chemistry gives 46.8 epfu. A higher measured site-scattering value (relative to that inferred from the WDS data) for *A** and a lower value for *B** appear to indicate that one (or more) of the strongly scattering cations is accommodated at *A**, albeit in minor quantities. If we filled the *A** site with Ce^{3+} (i.e. the cation closest to Ca and Na in size; Shannon, 1976), this would give total assigned site-scattering values of 16.6 epfu for *A** and 46.3 epfu for *B**, which is in good agreement with the experimentally determined values. We recognize that this is not conclusive evidence for minor Ce (± other REE) at *A**, but the likelihood of this occurring is noteworthy.

Structure description

The structure of carbocernaite comprises chains of edge-sharing A^*O_7 polyhedra and zigzag chains of face-sharing $(B,B')O_{10}$ polyhedra running parallel to the **b** axis. The A^*O_7 polyhedra are best described as a monocapped triangular prism with a mean cation-oxygen distance of ~2.44 Å, which is in excellent agreement with the value calculated from the ionic radii of Ca^{2+} and Na^{+} inferred to occupy the *A* and *A*' sites (2.44 Å: Shannon, 1976). This type of coordination is not uncommon in Ca and Na inorganic and organic compounds (e.g., Dickens and Bowen 1971; Lee and Harrison, 2004). The B^*O_{10} polyhedra are truncated hexagonal bipyramids similar to those hosting lanthanides in orthorhombic $LREE(CO_3)OH$ (Tahara et al. 2007), cordylite (Mills et al. 2012) and many other minerals, and Ba in mckelveyite-(Y) (Demartin et al. 2008). The mean measured cation-oxygen distance (~2.64 Å) is, again, in perfect accord with that calculated from the ionic radii of the (*B*,*B*') site occupants in a tenfold coordination (see

above). The polyhedral chains are interconnected by sharing vertices, edges and also via carbonate groups oriented parallel to (250) and (-2-50) (Fig. 5a). The structure can also be viewed as corrugated layers of B^*O_{10} bipyramids alternating with isolated chains of A^*O_7 capped prisms along the **a** axis (Fig. 5b). With the exception of site-splitting and lower symmetry, our results confirm the overall topology and cation coordinations determined by Voronkov and Pyatenko (1967); we found no evidence of lower (Sr,REE,Ba) coordination proposed by Shi et al. (1982).

Topologically, carbocernaite differs from all other anhydrous carbonates, including burbankite-group minerals (Onac et al. 2009). Corrugated polyhedral layers hosting large cations (Ba) and chains of CaO_7 monocapped triangular prisms are found in the structure of barytocalcite, $CaBa(CO_3)_2$ (Dickens and Bowen 1971). However, edge-sharing BaO_{11} polyhedra within the layer and CaO_7 polyhedra within the chain are arranged in a chessboard-like fashion, and successive layers are not trussed together with carbonate groups as in carbocernaite (Fig. 5c).

RAMAN SPECTROSCOPY

Raman spectra were acquired in confocal mode using a LabRAM ARAMIS instrument equipped with a 460-mm focal length spectrometer, multichannel electronically cooled CCD detector, motorized x-y-z stage, and solid-state 532-nm laser. An Olympus microscope coupled to the spectrometer was used to focus the laser beam on the sample surface and collect the generated Raman signal with a spatial resolution of ~1 μm. All spectra were collected with a diffraction grating of 1800 gr/mm, whereas other instrumental parameters were optimized to bring spectral resolution close to 1 cm^{-1}. The spectrometer was calibrated using a synthetic Si standard. In addition to the three compositionally distinct zones in the carbocernaite crystal shown in Figure 2a, spectra of burbankite and ancylite-(Ce) from the same sample were measured using the same instrumental parameters.

The spectra of the core, pyramidal and prismatic zones in carbocernaite show a number of consistent features (e.g., the presence of two intense Raman modes at ~1080 and 1100 cm^{-1} shouldered by a wide signal at ~980 cm^{-1}), as well as some differences (see below). Spectroscopically, the Ca-Sr-rich core and the most Na-LREE-rich pyramidal sector ("A" and "H", respectively, in Fig. 6a) differ from each other the most, whereas the compositionally intermediate prismatic zones yield a transitional type of spectrum. The Raman spectrum of the Ca-Sr-rich core material is distinctly different from those of ancylite-(Ce) and burbankite, particularly in the 900-1100 cm^{-1} range (Fig. 6b). Clearly, the three minerals can be readily distinguished on the basis of their Raman characteristics, even if their energy-dispersive spectra are inconclusive (see **INTRODUCTION**).

The peaks at ~1080 and 1100 cm^{-1} in the carbocernaite spectrum (Fig. 6a) can be confidently identified as symmetric C–O stretching modes (ν_1), and those between 690 and 740 cm^{-1} as O–C–O in-plane bending (ν_4) modes (e.g., Scheetz and White 1977). The observed splitting of the carbonate modes is undoubtedly due to the presence of four types of carbonate groups bonded to different cations in the structure (cf. benstonite spectrum in Scheetz and White 1977). That the splitting is particularly conspicuous in spectrum "H" suggests that cation ordering and, as a consequence, differences among the symmetrically non-equivalent carbonate groups increase with the Na and REE contents. Lattice translation modes between 120 and 270 cm^{-1} also differ in the two spectra, as can be expected from the different cation populations in these areas (Table 3). The broad signal at ~980 cm^{-1} is difficult to interpret because of the paucity of spectroscopic data for structurally complex carbonates. However, it is noteworthy that the same feature is present in the spectrum of the Bear Lodge burbankite (Fig. 6b) and has also been observed by other researchers in the spectra of disordered and ordered burbankite-type phases from other localities, measured under different instrumental conditions (see burbankite, calcioburbankite, petersenite and rémondite in the RRUFF database: Lafuente et al. 2015). Clearly, the possibility that the 980 cm^{-1} signal is an artefact can be safely ruled out. Because neither carbocernaite

nor burbankite-type phases contain anionic species other than $(CO_3)^{2-}$, the most likely cause of this spectroscopic feature is C–O interactions of lower energy than the symmetric stretching vibrations. A similar band has been reported in alkali-carbonate solutions under pressure, and interpreted as "the $\nu_1(A_1)$ mode of CO_3 species with significantly weaker C-O bonds due to M^+ - CO_3^{2-} association" (Zotov and Keppler 2000), but it remains to be seen whether this interpretation is relevant to crystalline Na-bearing carbonates.

DISCUSSION

Genesis of carbocernaite at Bear Lodge

The whole-rock trace-element and isotopic characteristics of the examined carbonatite sample (Table 1) are consistent with a mantle-derived magmatic origin. However, the available petrographic evidence (cavernous texture, secondary zoning in calcite, nearly pervasive replacement of primary burbankite, the abundance of ancylite among the alteration products), and the enrichment of the late-stage rhombohedral calcite in heavy O relative to the primary variety all indicate that the rock underwent low-T hydrothermal reworking (Zaitsev et al. 2002; Demény et al. 2004). Interaction of the primary carbonates (burbankite and calcite) with the fluid released Na, Ca, Sr, REE and Ba that were subsequently sequestered by hydrothermal phases precipitated in dissolution cavities [carbocernaite, strontianite, barite, ancylite-(Ce) and, to a lesser extent, late-stage calcite].

The subchondritic δCe, δEu and Y/Ho ratios of the Bear Lodge carbocernaite are lower than the whole-rock and primary calcite values, lending further support to its hydrothermal origin. A similar depletion in Eu and Y has been documented in burbankite from carbonatite-derived fluid inclusions at Kalkfeld, Namibia (Bühn et al. 1999), although the mechanism of Eu and Y fractionation has not been discussed in that work. Cerium, Eu and Y anomalies are well-known in submarine hydrothermal systems, where variations in their relative sense (positive/negative) and magnitude are interpreted from the

standpoint of source signature, fluid speciation, and preferential removal of specific REE by coprecipitation and scavenging (Bao et al. 2008 and references therein). Because the primary mineral paragenesis at Bear Lodge shows no Ce depletion (Table 1), the low δCe values of carbocernaite could develop due to the oxidizing character of the late-stage fluid and conversion of the released Ce^{3+} to insoluble Ce^{4+}. Although cerianite (CeO_2) is indeed common in the Fe-Mn-oxide (lateritic) zone of the deposit (Moore et al. 2015; Ray and Clark 2015), we observed none in the present sample, which was collected ~250 m below the inferred oxidation front. Moreover, the sulfide minerals in the examined carbonatite bear no signs of oxidation, whereas the replacement of marcasite by pyrite in the crystallization sequence (Fig. 1c) implies an increase in pH (Qian et al. 2011). Because barite precipitation in this mineral association required the presence of sulfate anions, it is feasible that the Ce-depleted, sulfate-bearing fluid was derived from the subsurface oxidized profile, where sulfide minerals locally making up a significant volume of the host carbonatite, were converted to Fe-Mn (hydr)oxides, and the Ce released from earlier-crystallized carbonates was partially sequestered in cerianite (Moore et al. 2015). The fluid could then percolate below the oxidation front, cause corrosion of the primary burbankite and calcite (Figs. 1a, 1b), and undergo partial reduction to form pyrite. Because of the low solubility of $BaSO_4$ in carbonate fluids (Bernard, 1973), the release of Ba from the primary phases triggered barite crystallization after the deposition of pyrite and carbocernaite in dissolution cavities (Fig. 1d). This model (Fig. 7) is in agreement with the low $\delta^{34}S_{V\text{-}CDT}$ value of pyrite (Table 1), which is to be expected in sulfides formed by sulfate reduction (Seal 2006; Magnall et al. 2016). Successive precipitation of pyrite and barite from sulfate-bearing fluids under low-T conditions has been previously reported in a number of studies (Goldberg et al. 2006; Magnall et al. 2016). This model, involving an externally derived fluid, is also consistent with the ^{18}O-enriched signature of the late-stage calcite associated with the carbocernaite (see **Occurrence and paragenesis**), and subchondritic δEu and Y/Ho values in the latter. Indeed, the negative shift in δEu and Y/Ho would be difficult to explain if the

examined carbonatite evolved as a closed system (e.g., through re-equilibration of the primary minerals with an orthomagmatic aqueous fluid). Primary calcite from carbonatites has near-chondritic δEu and Y/Ho ratios (Chakhmouradian et al. 2016; this work) and, thus, should not lead to Eu-Y depletion in a conjugate fluid. That the carbonatite as a whole retained its primary radiogenic isotopic signature (Table 1) owes to its overall enrichment in Sr and Nd (> 50000 and ~8000 ppm, respectively), which would effectively dwarf any potential crust-derived Sr- or Nd-isotopic contribution.

Crystal chemistry (solid solutions, miscibility and structural relations)

Our data, combined with those in the literature, show the existence of an extensive solid solution between the two principal end-members, $CaSr(CO_3)_2$ and $NaCe(CO_3)_2$ (Figs. 3a, 3b). With the exception of one Vuoriyarvi sample containing 0.18 apfu Ba (Wall and Zaitsev 2004), the proportion of $CaBa(CO_3)_2$ or other hypothetical end-members (e.g., those with Th or cation vacancies) is < 9 mol.%. The Weishan material, described by Zhang et al. (1995, p. 91) falls well off this main trend owing to its higher-than-expected proportion of Ca for the given Sr content (0.80 and 0.39 apfu, respectively), and to the significant excess of Na and Ca (1.13 apfu) over the ideal occupancy in the *A** sites. However, this mineral was analyzed by "wet-chemical" techniques and found to also contain 0.28 wt.% Mn and 3.77 wt.% H_2O, implying sample contamination. The majority of carbocernaite compositions reported in the literature are dominated by $CaSr(CO_3)_2$ (44-64 mol.%), but Pekov and Podlesnyi's (2004) analysis #2 from Khibiny gives 51mol.% $NaCe(CO_3)_2$ and 44 mol.% $CaSr(CO_3)_2$. The most LREE-rich zones in the Bear Lodge crystals also contain mol.% $NaCe(CO_3)_2$ > mol.% $CaSr(CO_3)_2$. Given the ordered distribution of cations in the structure (Voronkov and Pyatenko 1967; this work), these compositions contain predominantly Na and LREE in the *A** and *B** sites, respectively, and thus correspond to a new species compositionally distinct from carbocernaite. Unfortunately, the dearth of this Na-LREE-dominant material precluded its detailed structural study required for a new mineral proposal.

The data presented in this work suggest that the carbocernaite structure is stable across the compositional range from at least ~70 to 40 mol.% $CaSr(CO_3)_2$. Whether it persists further toward the end-member compositions, or not, is unknown. Pure $CaSr(CO_3)_2$ has been prepared in a few studies (e.g., Schultze-Lam and Beveridge 1994), but no structural data for this compound have been published. A natural carbonate approaching this binary composition (51-53 mol.% $CaCO_3$) has been reported by Wall et al. (1993) as Ca-rich strontianite, but no diffraction or spectroscopic data was provided to support that interpretation. Experimental studies of the series $CaCO_3$–$SrCO_3$ at T < 100 ^{o}C and ambient pressure (Plummer and Busenberg 1987) identified a wide miscibility gap between ~10 and ~60 mol.% $SrCO_3$. For a given T, this gap shrinks with increasing P, yielding a continuous series of strontianite-structured carbonates stable to ~400 ^{o}C at P = 10 kbar (Chang 1971). Clearly, further studies of intermediate Ca-Sr carbonates at ambient conditions are desirable. Simple binary Na-LREE carbonates have been synthesized at elevated CO_2 pressure and by dehydration of their hydrous counterparts (Schweer and Seidel 1981). The X-ray diffraction patterns of $NaLREE(CO_3)_2$ (LREE = La ... Sm) can be indexed on an orthorhombic cell (a = 6.405, b = 5.140, c = 7.163 Å when LREE = Ce), which is metrically similar to the carbocernaite cell (Table 4). Unfortunately, no other crystallographic data were provided in that experimental study.

IMPLICATIONS

In the present work, we expand the limits of solubility between the two end-members defining the compositional series $CaSr(CO_3)_2$ – $NaCe(CO_3)_2$. The Na-Ce-dominant members of this series represent a new species distinct from the Ca-Sr-dominant carbocernaite. In common with other LREE carbonates, we anticipate that La and Nd may also be present as a dominant *B*-site cation in natural compositions, further expanding the carbocernaite group membership. It is likely that the carbocernaite structure type persists to the Na-LREE end-member compositions (as suggested by the experimental findings of

Schweer and Seidel, 1981), but the point of carbocernaite-to-aragonite structural transition with increasing Ca and Sr contents remains to be determined. The absolute majority of carbocernaite compositions contain < 10 mol.% $CaBa(CO_3)_2$, even in those cases where appreciable Ba^{2+} was available in the crystallization environment (e.g., at Bear Lodge). Our data also suggest that the solubility limit of this component decreases with increasing Na and LREE contents (Fig. 3c), implying that the incorporation of Ba in this mineral is ionic-radius controlled. This interpretation is consistent with the structural differences between carbocernaite and barytocalcite: in order to accommodate the 12% difference in size between Sr^{2+} and Ba^{2+} (Shannon 1976), the cation polyhedra and carbonate groups in the latter are completely re-arranged, breaking the structure topology (Fig. 6c). This is in contrast to the more flexible burbankite structure, where variations in ionic radius among the principal constituent cations (Na, Ca, Sr, LREE, Ba) are accommodated through cation ordering and changes in coordination (Grice et al. 1994).

Anhydrous Na-REE carbonates do not precipitate readily from aqueous solutions, which instead yield tetragonal $NaREE(CO_3)_2 \cdot nH_2O$ phases (Mochizuki et al. 1974, Philippini et al. 2008). Clearly, elevated $P(CO_2)$ is required to prevent hydration and stabilize $NaREE(CO_3)_2$ (Schweer and Seidel 1981). Hydrothermal experiments of Nikol'skaya and Dem'yanets (2005) also indicate that high concentrations of Na_2CO_3 are required to precipitate this phase in the absence of catalysts, and that lower concentrations yield bastnäsite-type carbonates. Late-stage crystallization of carbocernaite, involving reaction of earlier-formed carbonates with a fluid (Wall and Zaitsev 2004; Drüppel et al. 2005; this work), could thus serve as an indicator of Na activity and $P(CO_2)$ if the effect of Ca and Sr substitutions on these parameters were constrained. Dissociation of $NaREE(CO_3)_2$ above ~500 ^{o}C (Nikol'skaya and Dem'yanets 2005) probably explains why, in contrast to burbankite (Zaitsev and Chakhmouradian 2002; Zaitsev et al. 2002), carbocernaite has not been documented as a primary magmatic phase. Further

experimental studies on the system $Na_2O–Ce_2O_3–CaO–SrO–CO_2–H_2O$ are desirable to ascertain relations among burbankite-, carbocernaite- and ancylite-type phases at the late stages of carbonatite evolution.

ACKNOWLEDGEMENTS

This work was supported by the Natural Sciences and Engineering Research Council of Canada, and Canada Foundation for Innovation (CFI). Rare Element Resources Ltd. is gratefully acknowledged for granting us access to their Bear Lodge property and exploration drill core. Associate Editor Hongwu Xu, Joel Grice and an anonymous reviewer are thanked for their expedient handling of, and valuable constructive comments on, the earlier version of this manuscript. We are also grateful to Frank C. Hawthorne for providing access to the CFI-funded X-ray facilities at the University of Manitoba.

REFERENCES CITED

Anders E. and Grevesse, N. (1989) Abundances of the elements – Meteoritic and solar. Geochimica et Cosmochimica Acta, 53, 197-214.

Baele, J.M., Monin, L., Navez, J., André, L. (2012) Systematic REE partitioning in cubo-dodecahedral fluorite from Belgium revealed by cathodoluminescence spectral imaging and laser ablation-ICP-MS. In M. Broekmans, Ed., Proceedings of the 10th International Congress for Applied Mineralogy, p. 23–30. Springer-Verlag, Berlin.

Bao, S., Zhou, H., Peng, X., Ji, F., and Yao, H. (2008) Geochemistry of REE and yttrium in hydrothermal fluids from the Endeavour segment, Juan de Fuca Ridge. Geochemical Journal, 42, 359–370.

Bernard, A.J. (1973) Metallogenic processes in intra-karstic sedimentation. In G.C. Amstutz and A.J. Bernard, Eds., Ores in Sediments, p. 43–57. Springer Verlag, Berlin, Germany.

Bhushan, S.K. and Kumar, A. (2013) First carbonatite hosted REE deposit from India. Journal of the Geological Society of India, 81, 41–60.

476 Bühn, G., Rankin, A.H., Radtke, M., Haller, M., and Knöchel, A. (1999) Burbankite, a (Sr,REE,Na,Ca)-
477 carbonate in fluid inclusions from carbonatite-derived fluids: Identification and characterization
478 using Laser Raman spectroscopy, SEM-EDX, and synchrotron micro-XRF analysis. American
479 Mineralogist, 84, 1117–1125.
480 Bulakh, A.G. and Izokh, E.P. (1967) New data on carbocernaite. Doklady Akademii Nauk SSSR, 175, 175-
481 177 (in Russian).
482 Bulakh, A.G., Kondrat'eva, V.V., and Baranova, E.N. (1961) Carbocernaite – a new rare-earth carbonate.
483 Zapiski Vsesoyuznogo Mineralogicheskogo Obshchestva, 90 (1), 42–49 (in Russian).
484 Burtseva, M.V., Ripp, G.S., Doroshkevich, A.G., Viladkar, S.G., and Varadan, R. (2013) Features of mineral
485 and chemical composition of the Khamambettu Carbonatites, Tamil Nadu. Journal of the Geological
486 Society of India, 81, 655–664.
487 Chakhmouradian, A.R., Reguir, E.P., Couëslan, C., and Yang, P. (2016) Calcite and dolomite in intrusive
488 carbonatites. II. Trace-element variations. Mineralogy and Petrology, 110, 361–377.
489 Chakhmouradian, A.R. and Wall, F. (2012) Rare earth elements: Minerals, mines, magnets (and more).
490 Elements, 8, 333–340.
491 Chang, L.L.Y. (1971) Subsolidus phase relations in the aragonite-type carbonates: I. The system $CaCO_3$-
492 $SrCO_3$-$BaCO_3$. American Mineralogist, 56, 1660–1673.
493 Costanzo, A., Moore, K.R., Wall, F., and Feely, M. (2006) Fluid inclusions in apatite from Jacupiranga
494 calcite carbonatites: Evidence for a fluid-stratified carbonatite magma chamber. Lithos, 91, 208–228.
495 Cressey, G., Wall, F., and Cressey, B.A. (1999) Differential *REE* uptake by sector growth of monazite.
496 Mineralogical Magazine, 63, 813–828.
497 Dal Negro, A., Rossi, G., and Tazzoli, V. (1975) The crystal structure of ancylite, $(RE)_x(Ca,Sr)_{2-}$
498 $_x(CO_3)_2(OH)_x(2\text{-}x)H_2O$. American Mineralogist , 60, 280–284.

Demartin, F., Gramacccioli, C.M., Campostrini, I. and Diella, V. (2008) The crystal structure of mckelvyite-(Y)-2*M*, a new monoclinic polytype from Val Malenco, Italian Alps. Canadian Mineralogist, 46, 195–203.

Demény, A., Sitnikova, M.A., and Karchevsky, P.I. (2004) Stable C and O isotope compositions of carbonatite complexes of the Kola Alkaline Province: phoscorite–carbonatite relationships and source compositions. In F. Wall and A.N. Zaitsev, Eds., Phoscorites and Carbonatites from Mantle to Mine: the Key Example of the Kola Alkaline Province, p. 407–431. Mineralogical Society, London.

Dickens, B. and Bowen, J.S. (1971) The crystal structure of $BaCa(CO_3)_2$ (barytocalcite). Journal of Research of the National Bureau of Standards, 75A, 197–203.

Drüppel, K., Hoefs, J., and Okrusch, M. (2005) Fenitizing processes induced by ferrocarbonatite magmatism at Swartbooisdrif, NW Namibia. Journal of Petrology, 46, 377–406.

Drüppel, K., Wagner, T., and Boyce, A.J. (2006) Evolution of sulfide mineralization in ferrocarbonatite, Swartbooisdrif, northwestern Namibia: constraints from mineral compositions and sulfur isotopes. Canadian Mineralogist, 44, 877-894.

Eremenko, G.K., and Vel'ko, V.A. (1982) Khanneshite $(NaCa)_3(Ba, Sr, TR, Ca)_3 (CO_3)_5$ - a new mineral of the burbankite group. Zapiski Vsesoyuznogo Mineralogicheskogo Obshchestva 111 (3), 321–324 (in Russian).

Farrell, S., Bell, K., and Clark, I. (2010) Sulphur isotopes in carbonatites and associated silicate rocks from the Superior Province, Canada. Mineralogy and Petrology, 98, 209–226.

Goldberg, T., Mazumdar, A., Strauss, H, and Shields, G. (2006) Insights from stable S and isotopes into biogeochemical processes and genesis of Lower Cambrian barite–pyrite concretions of South China. Organic Geochemistry, 37, 1278-1288.

Grice, J.D., Van Velthuizen, J., and Gault, R.A. (1994) Petersenite-(Ce), a new mineral from Mont saint-Hilaire, and its structural relationship to other REE carbonates. Canadian Mineralogist, 32, 405–414.

Harris, D.C. (1972) Carbocernaite, a Canadian occurrence. Canadian Mineralogist, 11, 812–818.

Herman, R.G., Bogdan, C.E., Sommer, A.J., and Simpson, D.R. (1987) Discrimination among carbonate minerals by Raman spectroscopy using the laser microprobe. Applied Spectroscopy, 41, 437–440.

Horváth, L. and Gault, R.G. (1990) The mineralogy of Mont Saint Hilaire. Mineralogical Record, 21, 284 359.

Lafuente, B., Downs, R.T., Yang, H., Stone, H. (2015) The power of databases: the RRUFF project. In T. Armbruster and R.M. Danisi, Eds., Highlights in Mineralogical Crystallography, p. 1–30. W. De Gruyter, Berlin, Germany.

Lee, C., and Harrison, W.T.A. (2004) The *catena*-arsenite chain anion, $[AsO_2]_n^{n-}$: $(H_3NCH_2CH_2NH_3)_{0.5}[AsO_2]$ and $NaAsO_2$ (revisited). Acta Crystallographica, C60, m215–m218.

Magnall, J.M., Gleeson, S.A., stern, R.A., newton, R.J., Poulton, S.W., and Paradis, S. (2016) Open system sulphate reduction in a diageetic environment – Isotopic analysis of barite ($\delta^{34}S$ and $\delta^{18}O$) and pyrite ($\delta^{34}S$) from the Tom and jason Late Devonian Zn–Pb–Ba deposits, Selwyn Basin, Canada. Geochimica et Cosmochimica Acta, 180, 146–163.

Mills, S.J., Kartashov, P.M., Kampf, A.R., Konev, A.A., Koneva, A.A. and Raudsepp, M. (2012) Cordylite-(La), a new mineral species in fenite from the Biraya Fe-REE deposit, Irkutsk, Russia. Canadian Mineralogist, 50, 725–734.

Mochizuki, A., Nagashima, K., and Wakita, H. (1974) The synthesis of crystalline hydrated double carbonates of rare earth elements and sodium. Bulletin of the Chemical Society of Japan, 47, 755-756.

Moore, M., Chakhmouradian, A.R., Mariano, A.N., and Sidhu, R. (2015) Evolution of rare-earth mineralization in the Bear Lodge carbonatite, Wyoming: Mineralogical and isotopic evidence. Ore Geology Reviews, 64, 499–521.

546 Nikol'skaya, O.G. and Dem'yanets, L.N. (2005) Hydrothermal crystallization in the systems
547 $La_2(CO_3)_3 \cdot 6H_2O$–$CaCO_3$–R-H_2O (R = Na_2CO_3, K_2CO_3, $NaHCO_3$, $KHCO_3$, NaCl, NH_4Cl, $CO(NH_2)_2$). Inorganic
548 Materials, 41, 1206–1212.
549 Noble, A.C., Clark, J.G., and Ranta, D.E. (2009) Technical report on the mineral resources of the Bear
550 Lodge rare-earths project. Prepared for Rare Element Resources Ltd, 173 p.
551 Noble, A.C., Pickarts, J.T., and Larsen, R.T. (2013) Technical report on the mineral reserves and resources
552 and development of the Bull Hill mine. Prepared for Rare Element resources Inc, 278 p.
553 Norman, M.D., Pearson, N.J., Sharma, A., and Griffin, W.L. (1996) Quantitative analysis of trace elements
554 in geological materials by laser ablation ICPMS: instrumental operating conditions and calibration of
555 NIST glasses. Geostandards Newsletter, 20, 247–261.
556 Onac, B.P., Bernhardt, H.-J., and Effenberger, H. (2009) Authigenic burbankite in the Cioclovina Cave
557 sediments (Romania). European Journal of Mineralogy, 21, 507–514.
558 Orris, G.J. and Grauch, R.I. (2002) Rare earth element mines, deposits, and occurrences. USGS Open-File
559 Report 02-189, 174 p.
560 Pekov, I.V. and Podlesnyi, A.S. (2004) Kukisvumchorr. Association Ecost, Moscow, Russia, 168 p.
561 Philippini, V., Vercouter, T., Chaussé, A., and Vitorge, P. (2008) Precipitation of $ALn(CO_3)_2,xH_2O$ and
562 $Dy_2(CO_3)_3,xH_2O$ compounds from aqueous solutions for $A^+ = Li^+, Na^+, K^+, Cs^+, NH_4^+$ and $Ln^{3+} = La^{3+}$,
563 Nd^{3+}, Eu^{3+}, Dy^{3+}. Journal of Solid State Chemistry, 181, 2143–2154.
564 Plummer, L.N. and Busenberg, E. (1987) Thermodynamics of aragonite-strontianite solid solutions:
565 results from stoichiometric solubility at 25 and 76°C. Geochimica et Cosmochimica Acta, 51, 1393–
566 1411.
567 Qian, G., Xia, F., brugger, J., Skinner, W.M., Bei, J., Chen, G., and Pring, A. (2011) replacement of
568 pyrrhotite by pyrite and marcasite under hydrothermal consitions up to 220 °C: An experimental
569 study of reaction textures and mechanisms. American Mineralogist, 96, 1878–1893.

570 Ray, J.T., and Clark, J.G. (2015) Exploration for REE and gold in the Bear Lodge Tertiary alkaline complex,
571 Crook County, Wyoming. In W.M. Pennell and L.J. Garside, Eds., New Concepts and Discoveries
572 (Geological Society of Nevada Symposium), p. 521–550. DESTech Publications, Inc., Lancaster, USA.
573 Reguir, E.P. and Mitchell, R.H. (2000) The mineralogy of carbonatites and related potassic syenites from
574 the Rocky Boy stock, Bearpaw Mountains, north-central Montana. GAC–MAC Annual Meeting
575 GeoCanada 2000, CD with Abstracts, file 374.PDF.
576 Scheetz, B.E. and White, W.B. (1977) Vibrational spectra of alkaline earth double carbonates. American
577 Mineralogist, 62, 36–50.
578 Schultze-Lam, S. and Beveridge, T.J. (1994) Nucleation of celestite and strontianite on a cyanobacterial S-
579 layer. Applied and Environmental Microbiology, 60, 447–453.
580 Schweer, H. and Seidel, H. (1981) Natrium-Lanthanoid-Carbonate. Zeitschrift für Anorganische und
581 Allgemeine Chemie, 477, 196–204.
582 Seal, R.R. (2006) Sulfur isotope geochemistry of sulfide minerals. Reviews in Mineralogy and
583 Geochemistry, 61, 633–677.
584 Shannon, R.D. (1976) Revised effective ionic radii and systematic studies of interatomic distances in
585 halides and chalcogenides. Acta Crystallogr A32:751–767.
586 Sheldrick, G.M. (2008) A short history of *SHELX*. Acta Crystallographica, A64, 112–122.
587 Shi, N., Ma, Z., and Peng, Z. (1982) The crystal structure of carbocernaite. Kexue Tongbao, 27, 76–80 (in
588 Chinese).
589 Staatz, M.H. (1983) Geology and description of thorium and rare-earth deposits in the southern Bear
590 Lodge Mountains, northeastern Wyoming. US Geological Survey Professional Paper, 1049-D, 52 p.
591 Tahara, T., Nakai, I., Miyawaki, R., and Matsubara, S. (2007) Crystal chemistry of RE(CO_3)OH. Zeitschrift
592 für Kristallografie, 222, 326–334.

Traversa, G., Gomes, C. B., Brotzu, P., Buraglini, N., Morbidelli, L., Principato, M. S. Ronca, S., and Ruberti, E. (2001) Petrography and mineral chemistry of carbonatites and mica-rich rocks from the Araxá complex (Alto Paranaíba Province, Brazil). Anais da Academia Brasileira de Ciências, 73, 71–98.

van Achterbergh, E., Ryan, C.G., Jackson, S.E., and Griffin, W.L. (2001) Data reduction software for LA–ICP–MS. In P. Sylvester, Ed., Laser-Ablation – ICPMS in the Earth Sciences, Principles and Applications, p. 239–242. Mineralogical Association of Canada, Short Course, Volume 29.

Voronkov, A.A. and Pyatenko, Yu.A. (1967) Crystal structure of carbocernaite (Na, Ca)(TR, Sr, Ca, Ba)$(CO_3)_2$. Journal of Structural Chemistry, 8, 835–840.

Wall, F., Le Bas, M.J., and Srivastava, R.K. (1993) Calcite and carbocernaite exsolution and cotectic textures in a Sr,*REE*-rich carbonatite dyke from Rajasthan, India. Mineralogical Magazine, 57, 495–513.

Wall, F. and Zaitsev, A.N. (2004) Rare earth minerals in Kola carbonatites. In F. Wall and A.N. Zaitsev, Eds., Phoscorites and Carbonatites from Mantle to Mine: the Key Example of the Kola Alkaline Province, p. 341–373. Mineralogical Society Series, London.

Zaitsev, A.N. and Chakhmouradian, A.R. (2002) Calcite-amphibole-clinopyroxene rock from the Afrikanda complex, Kola Peninsula, Russia: Mineralogy and a possible link to carbonatites. II. Oxysalt minerals. Canadian Mineralogist, 40, 103–120.

Zaitsev, A.N., Demény, A., Sindern, S., and Wall, F. (2002) Burbankite group minerals and their alteration in rare earth carbonatites – source of elements and fluids (evidence from C–O and Sr–Nd isotopic data). Lithos, 62, 15–33.

Zhang, P., Yang, Z., Kejie, T., and Yang, X. (1995) Mineralogy and Geology of Rare earths in China. Science Press, Beijing, 235 p.

Zotov, N. and Keppler, H. (2000) Effects of pressure and temperature on aqueous carbonate fluids. Bayerisches Forschungsinstitut für Experimentelle Geochemie und Geophysik, Universität Bayreuth, Annual Report 2000, report 3.4h.

FIGURE CAPTIONS

FIGURE 1. False-color BSE images showing major textural and mineralogical characteristics of the carbocernaite-bearing carbonatite from Bear Lodge; scale bar is 50 μm for (a), (b) and (e), and 200 μm for the rest of the images. (a) Magmatic fluorapatite (Fap) and partially resorbed burbankite (Brb) enclosed in Mn-Fe-rich primary calcite (Cal1); note zoning in the burbankite involving Ba enrichment in the rim. (b) Cavernous pseudomorph after burbankite lined with sub- to euhedral late-stage Sr-Ba-rich calcite (Cal2), strontianite (Str) and ancylite-(Ce) (Anc). (c) Dissolution cavity lines with euhedral pyrite (Py) (note relict marcasite, Mrc, in the core), carbocernaite (Crb) and strontianite; note the lack of any evidence of sulfide oxidation. (d) Cluster of zoned, euhedral carbocernaite crystals associated with anhedral strontianite and barite (Brt). (e) Euhedral carbocernaite locally replaced and overgrown by ancylite. (f) Dissolution cavity in primary calcite filled with carbocernaite and barite (indistinguishable at that contrast level); note secondary zoning in the calcite along fluid passageways.

FIGURE 2. Grayscale BSE images showing zoning in carbocernaite crystals (scale bar is 200 μm for all images) and the location of areas analyzed by: WDS (10 μm; small circles, numbered as in Table 2), LA-ICPMS (30 μm; large circles, lettered as in Table 3), Raman (1 μm; stars), and single-crystal X-ray diffraction (80 μm; diamond).

FIGURE 3. Compositional variation of carbocernaite from Bear Lodge (diamonds) and other localities (Wall et al. 1993; Zhang et al. 1995; Pekov and Podlesnyi 2004; Wall and Zaitsev 2004). (a) Sr vs. Ca (apfu calculated to six atoms of oxygen); (b) REE vs. Na (apfu); (c) REE vs. Ba (wt.%); (d) $(La/Er)_{cn}$ vs. Sr/Na (normalization values from Anders and Grevesse, 1989); the logarithmic correlation between these two parameters in the growth sectors has an R^2 of 0.62; (e) representative chondrite-normalized patterns of the three major zone types in the Bear Lodge crystals. Note that the medium- and high-AZ sectors (Fig. 2) are referred to here as prismatic and pyramidal, respectively, in a morphological, not crystallographic, sense.

FIGURE 4. The 0*kl* plane of measured intensities transformed into precession geometry for carbocernaite fragment from location 5 (Fig. 2b). Red arrows mark observed reflections with *k* = odd that violate the *b*-glide and 2_1 screw axis in $Pb2_1m$ (space group determined by Voronkov and Pyatenko 1967).

FIGURE 5. The crystal structure of carbocernaite; two types of sevenfold- and tenfold-coordinated cations are grouped as *A** and *B**, respectively (see *Structure refinement*). (a) Chains of A^*O_7 and layers of B^*O_{10} polyhedra, viewed at a small angle to **b**; back edges are shown only for two polyhedra to avoid clutter. (b) A "Swiss-cheese" layer of B^*O_{10} polyhedra and chains of A^*O_7 aligned parallel to *b*, viewed at a small angle to **a**. (c) Comparison between the structures of carbocernaite and barytocalcite (Dickens and Bowen 1971); both viewed perpendicular to the layers of large cation polyhedra.

FIGURE 6. Representative Raman spectra of Ca-Sr-REE carbonates from Bear Lodge: (a) Ca-Sr-rich and Na-REE-rich varieties of carbocernaite (locations A and H, respectively, in Fig. 2a); (b) spectrum of Ca-Sr-rich carbocernaite compared with those of ancylite-(Ce) and burbankite, which exhibit similar EDS spectra (see text).

663

664 **FIGURE 7.** Genetic model for the carbocernaite-bearing carbonatite at Bear Lodge (see **DISCUSSION**). Cer =

665 cerianite-(Ce), Mnz = monazite-(Ce), other abbreviations as in Figure 1.

This is a preprint, the final version is subject to change, of the American Mineralogist (MSA)
Cite as Authors (Year) Title. American Mineralogist, in press.
(DOI will not work until issue is live.) DOI: http://dx.doi.org/10.2138/am-2017-6046

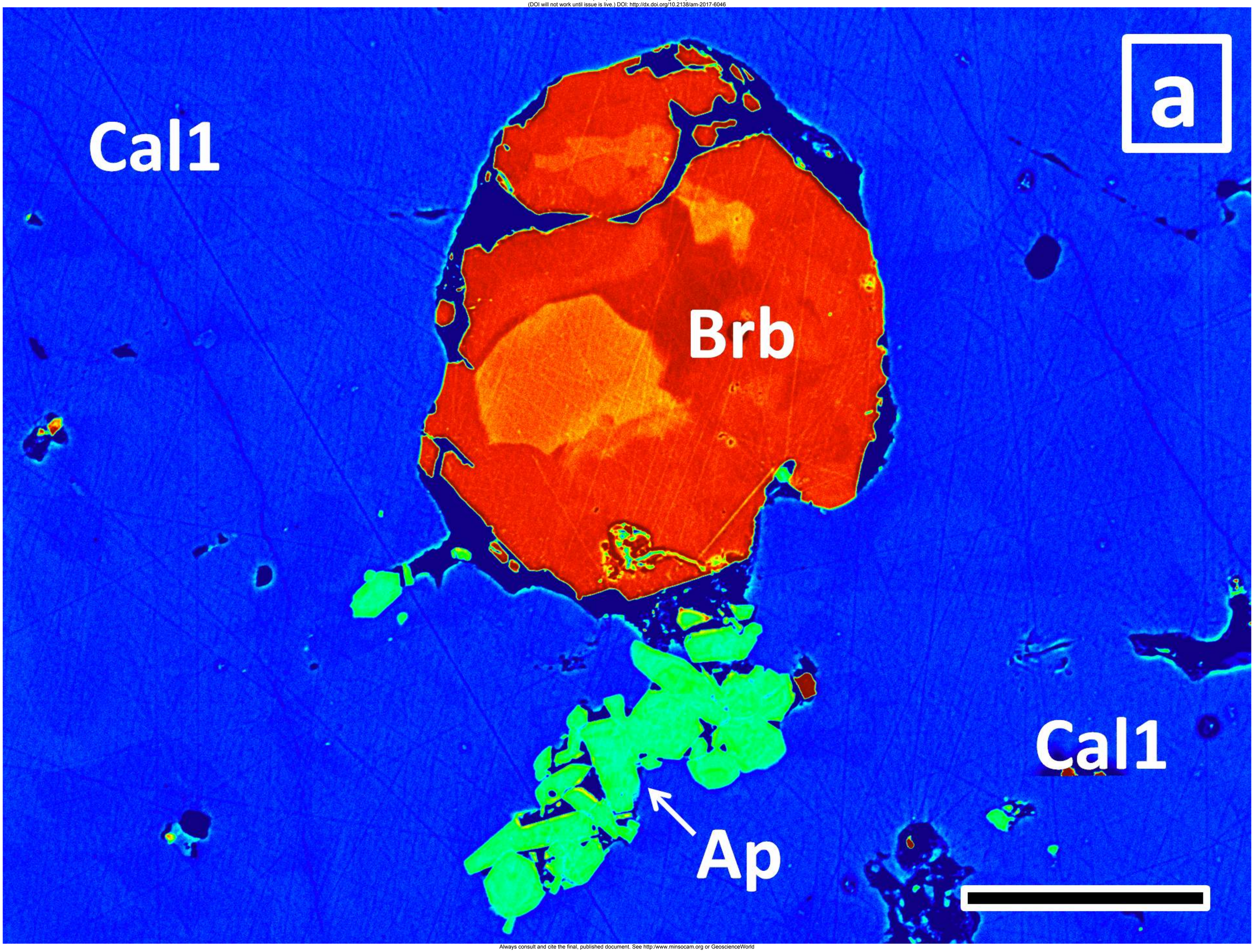

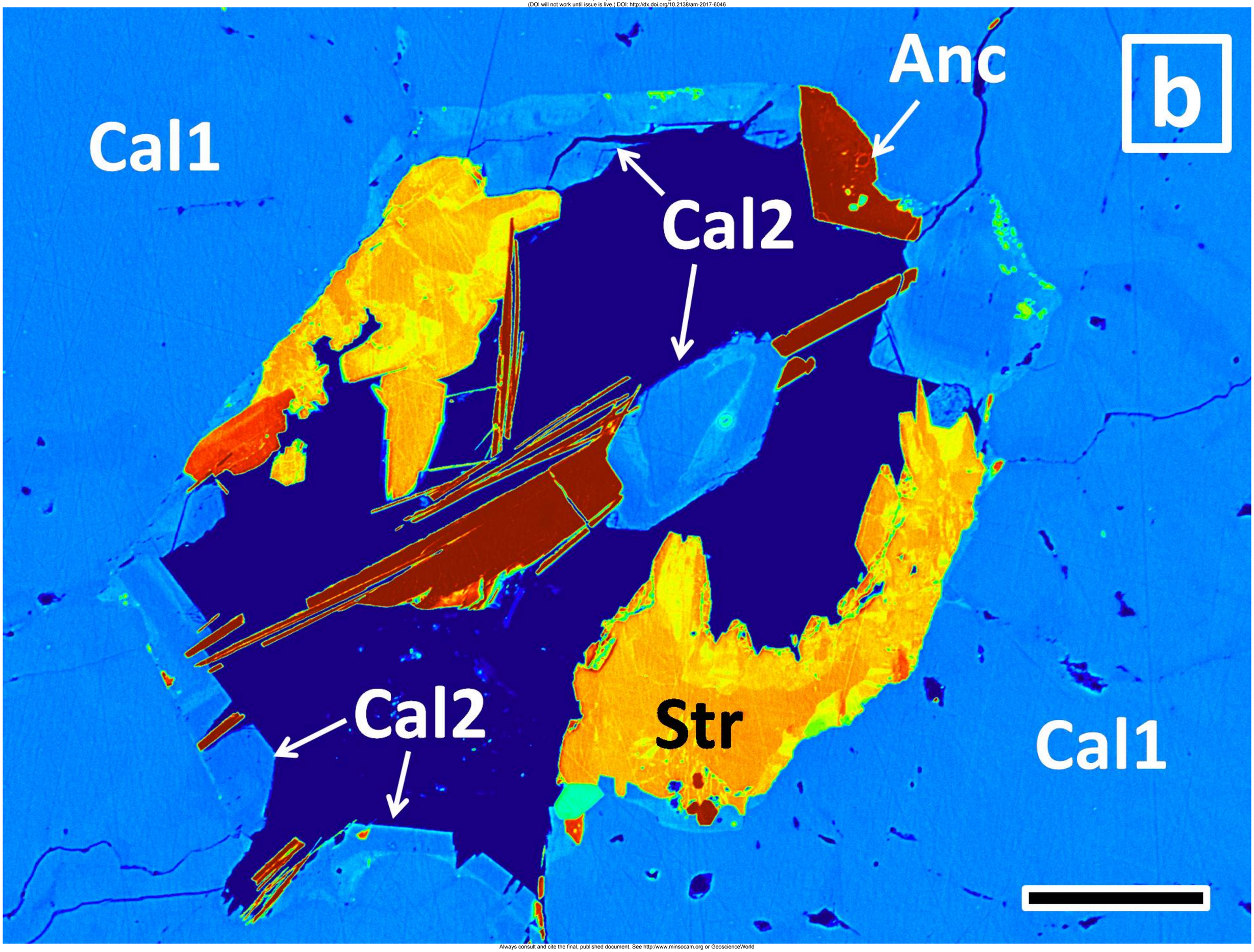

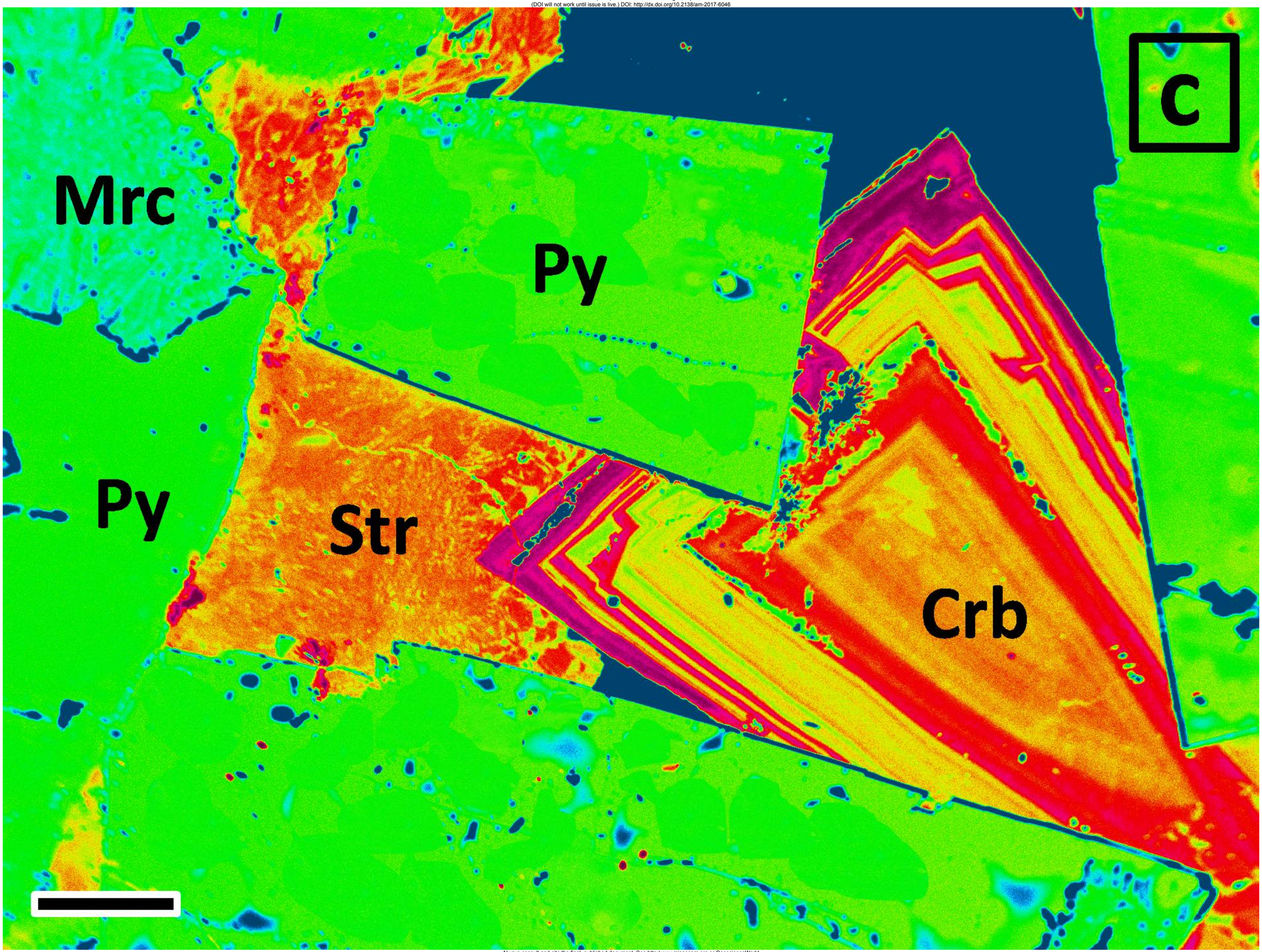

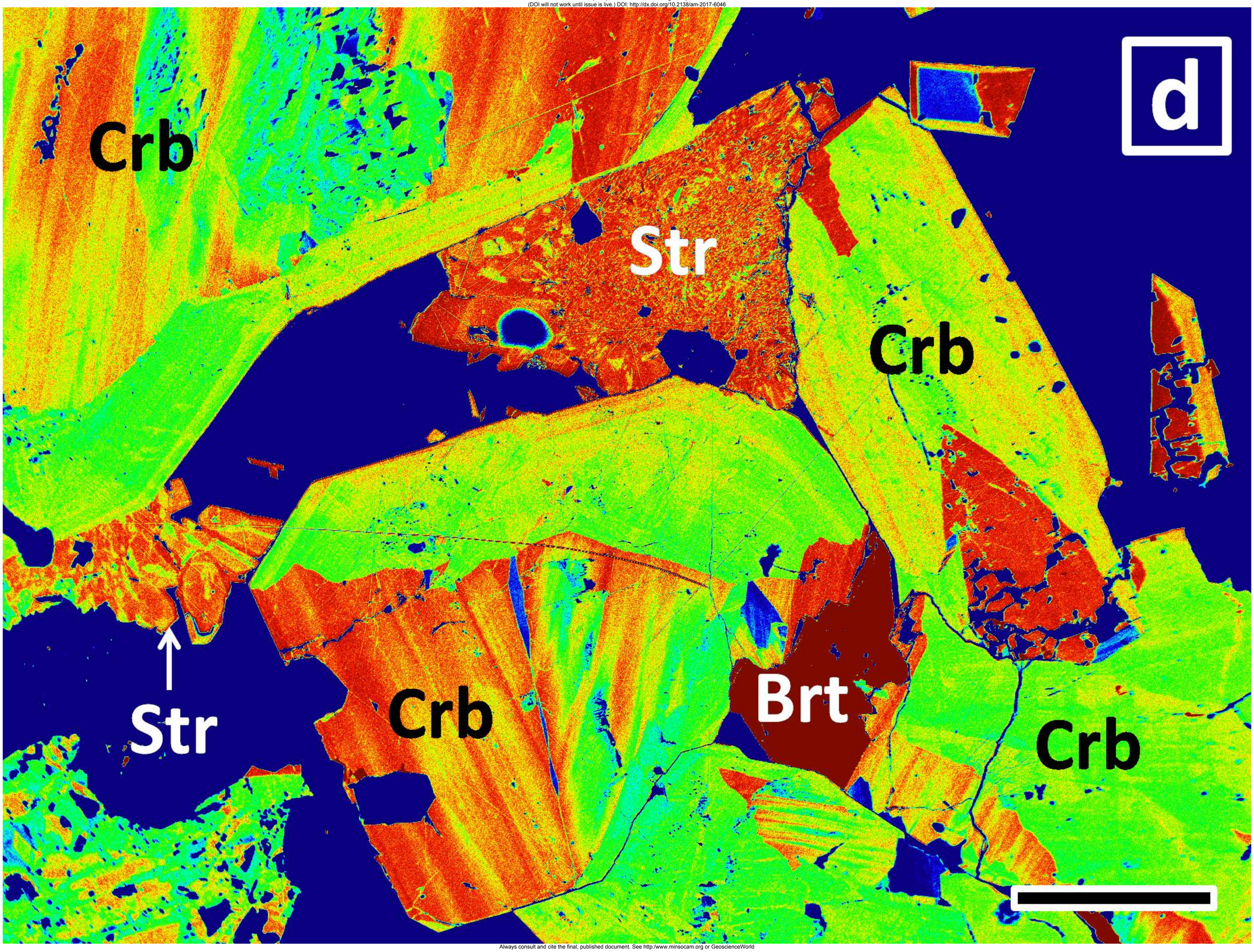

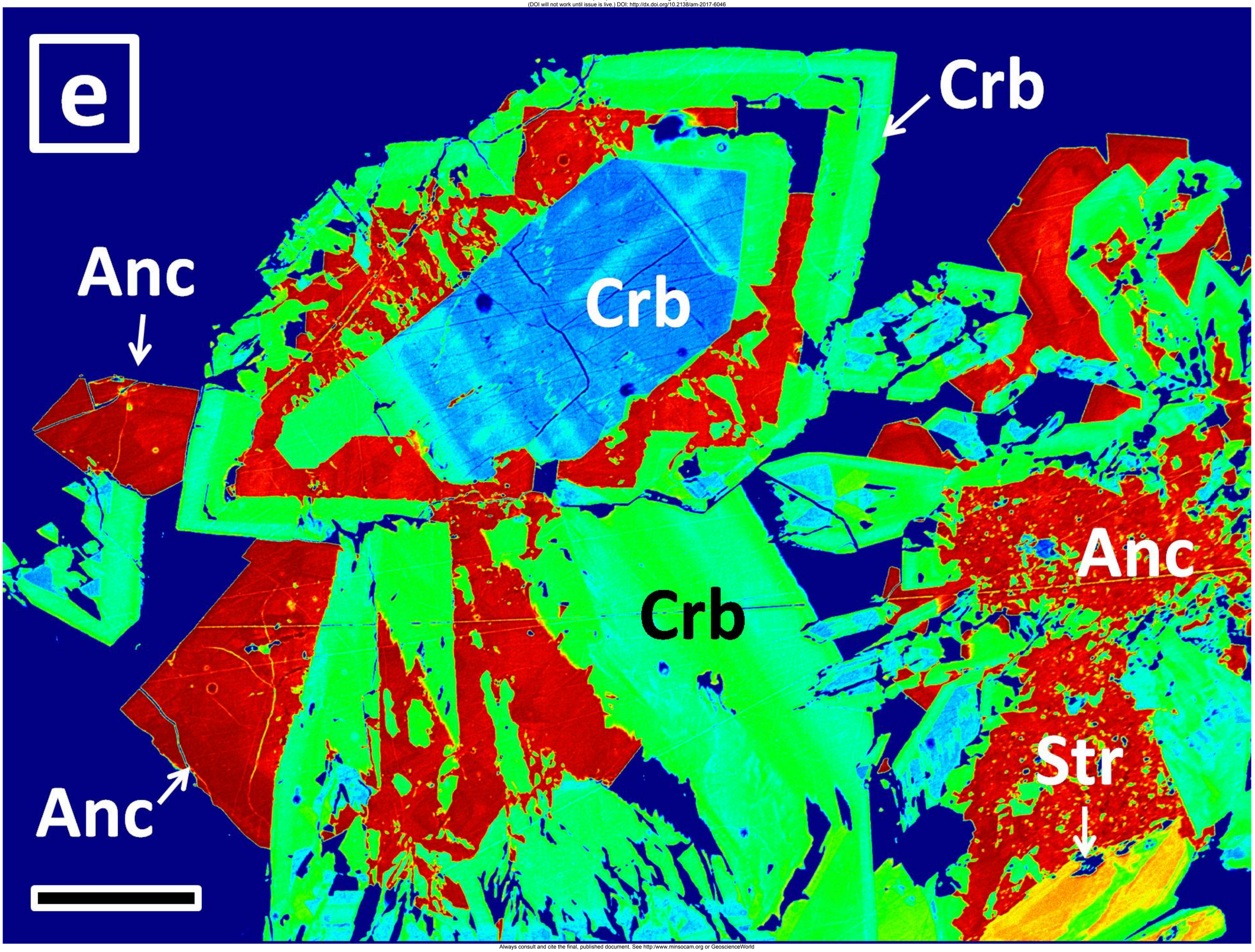

This is a preprint, the final version is subject to change, of the American Mineralogist (MSA)
Cite as Authors (Year) Title. American Mineralogist, in press.
(DOI will not work until issue is live.) DOI: http://dx.doi.org/10.2138/am-2017-6046

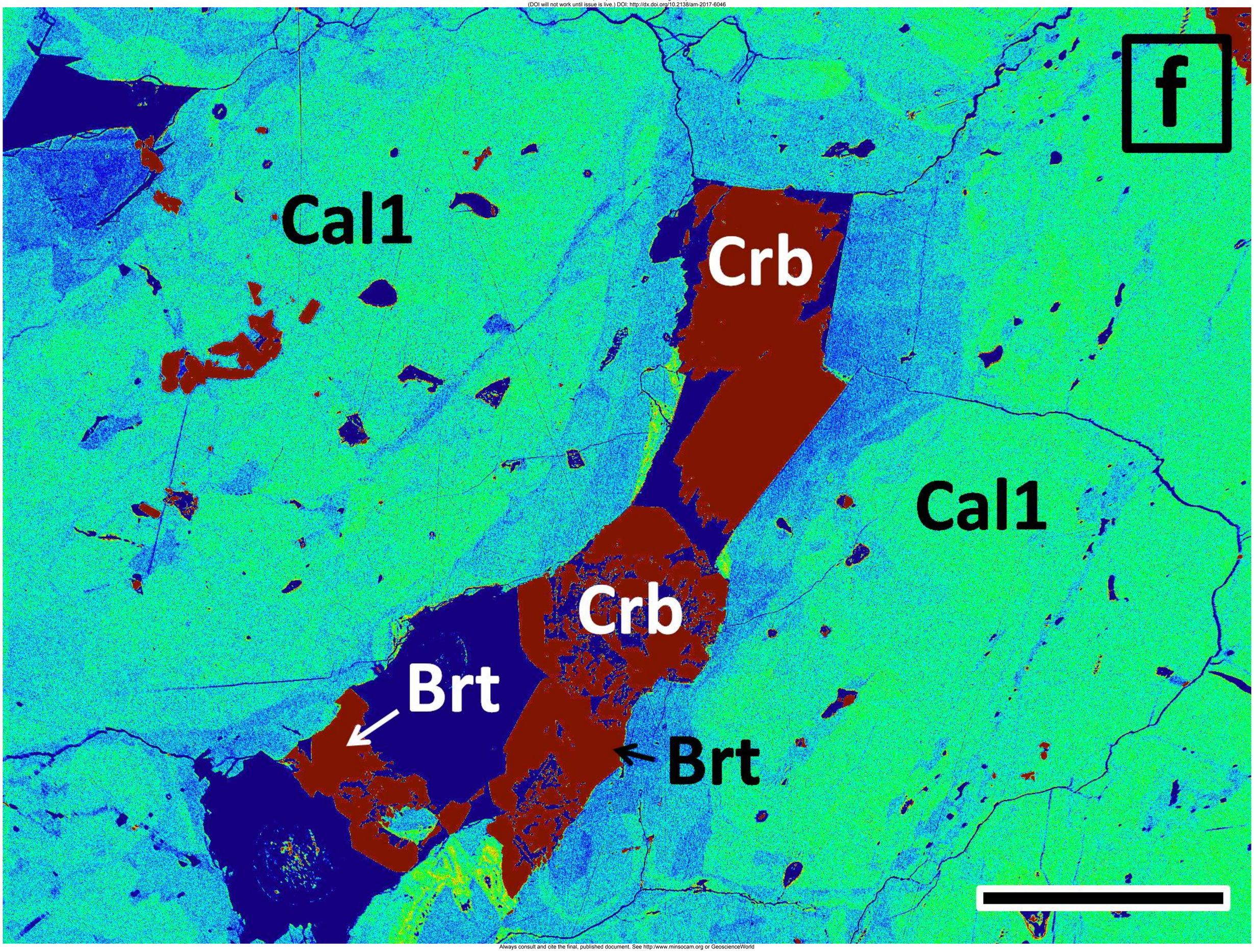

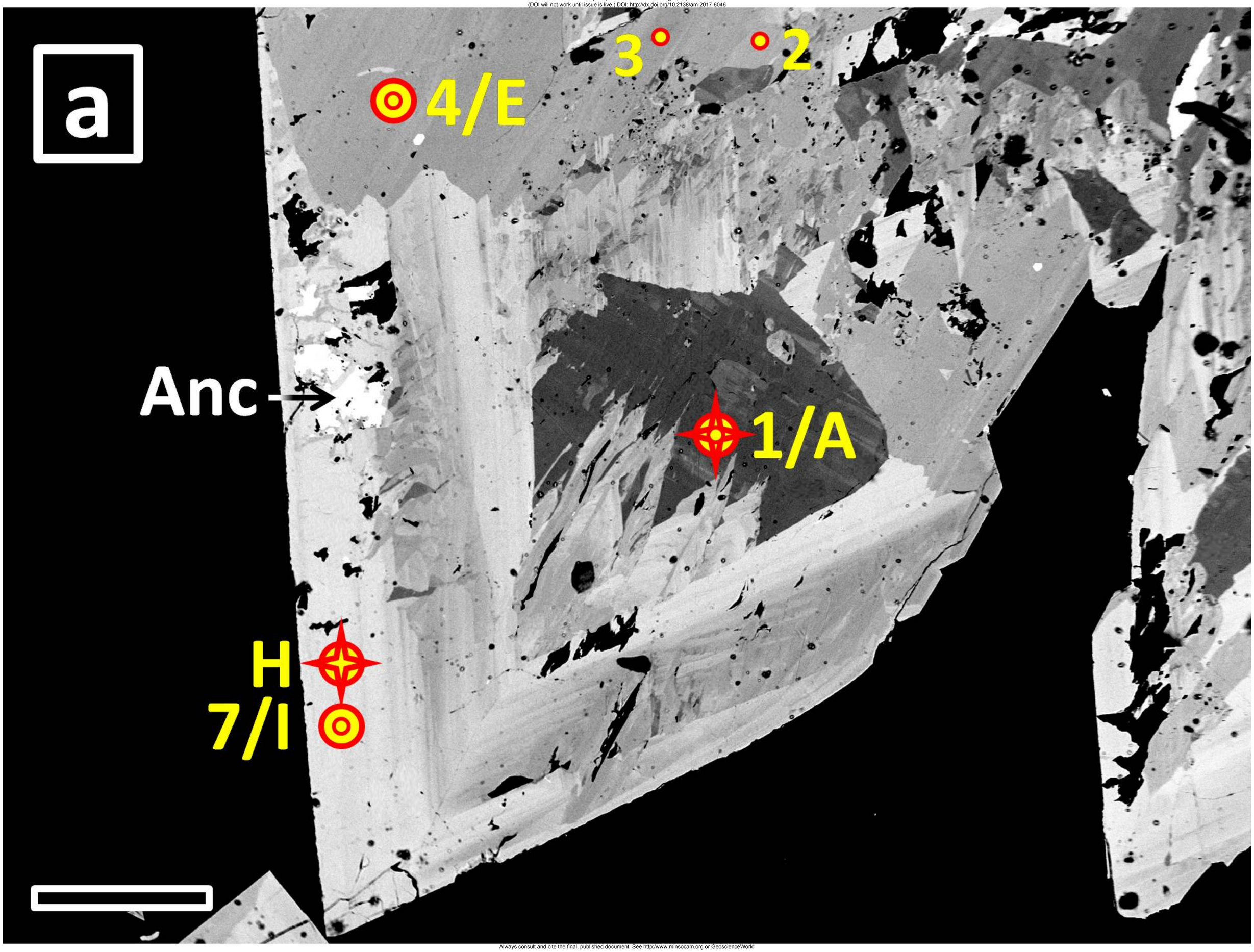

This is a preprint, the final version is subject to change, of the American Mineralogist (MSA)
Cite as Authors (Year) Title. American Mineralogist, in press.
(DOI will not work until issue is live.) DOI: http://dx.doi.org/10.2138/am-2017-6046

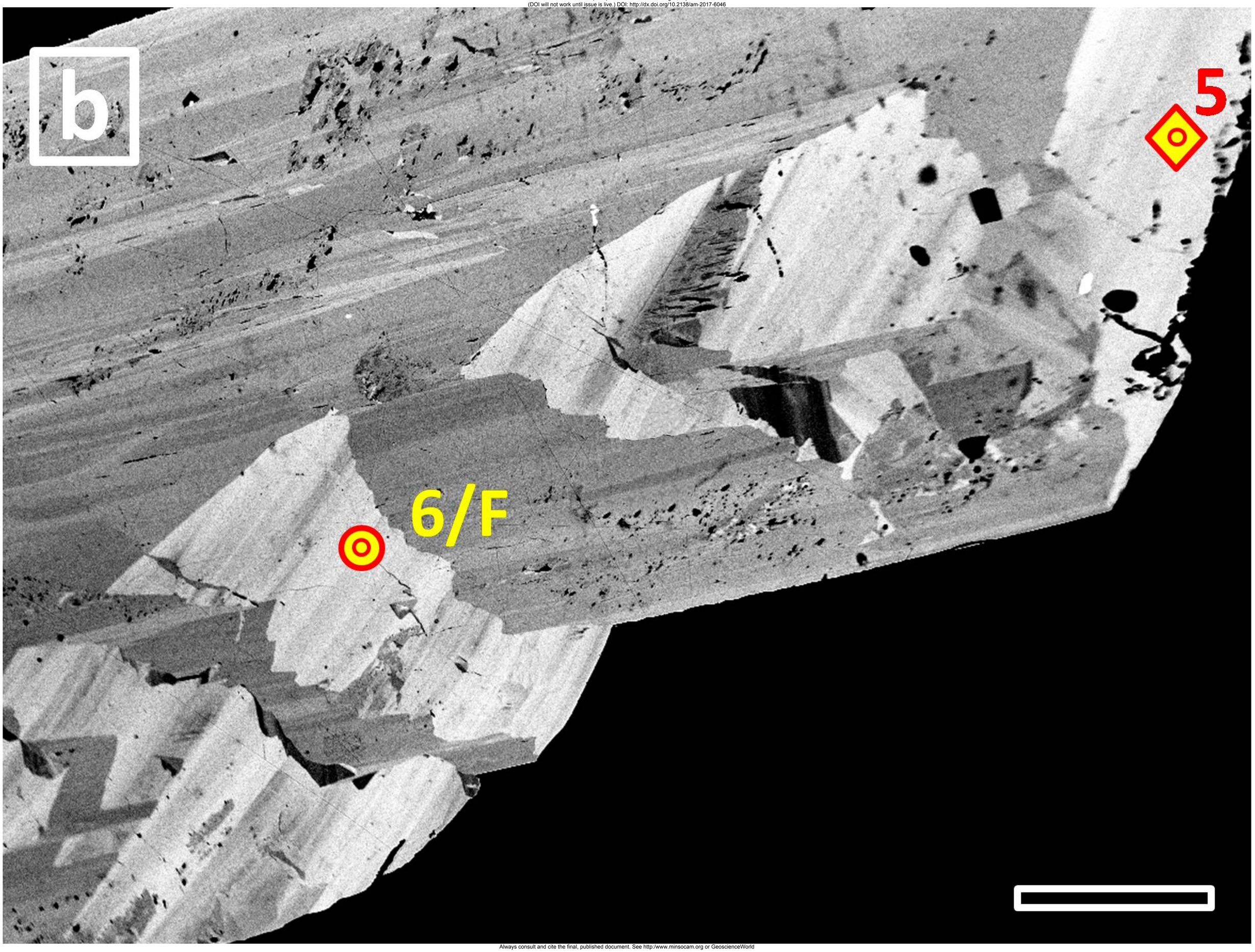

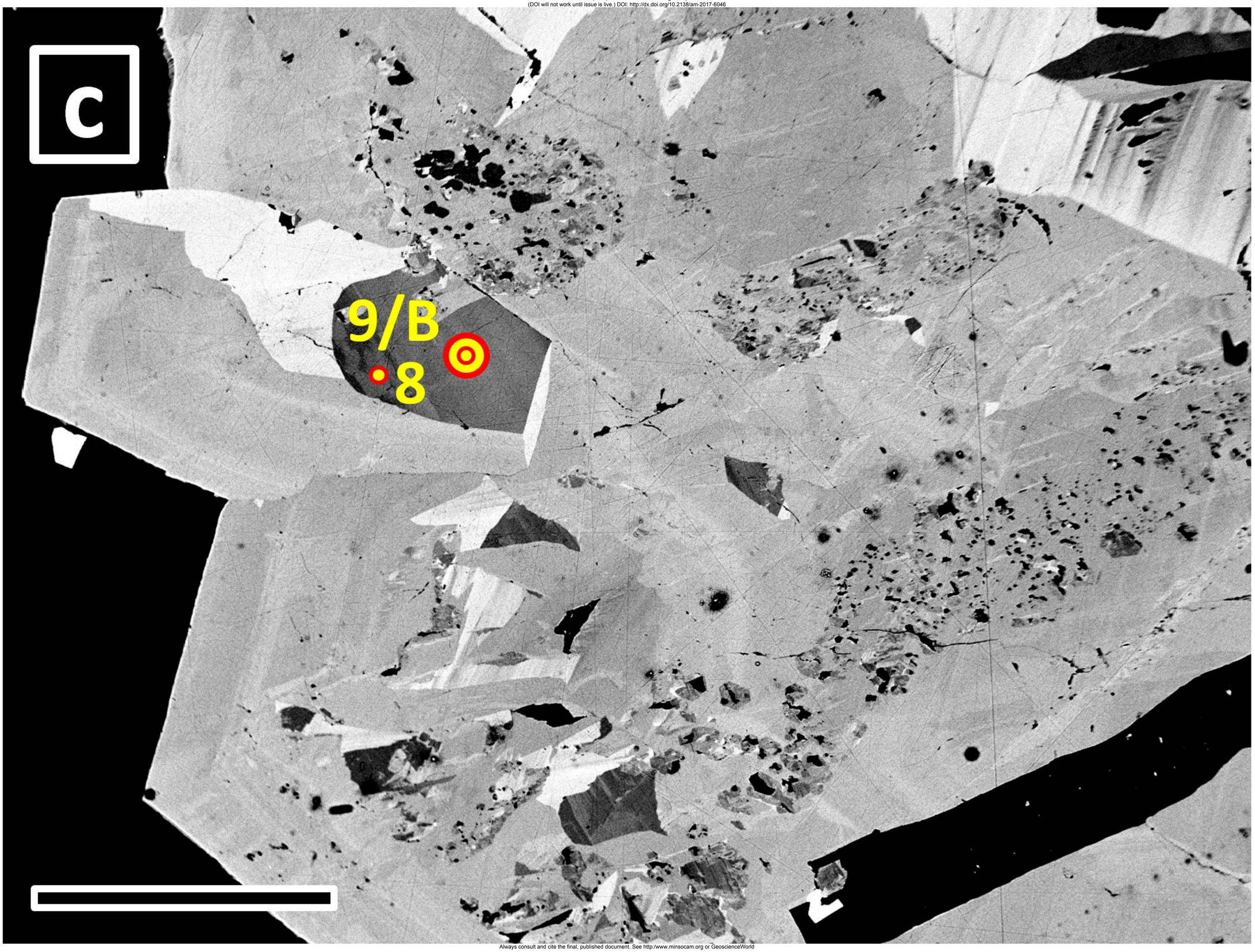

This is a preprint, the final version is subject to change, of the American Mineralogist (MSA)
Cite as Authors (Year) Title. American Mineralogist, in press.
(DOI will not work until issue is live.) DOI: http://dx.doi.org/10.2138/am-2017-6046

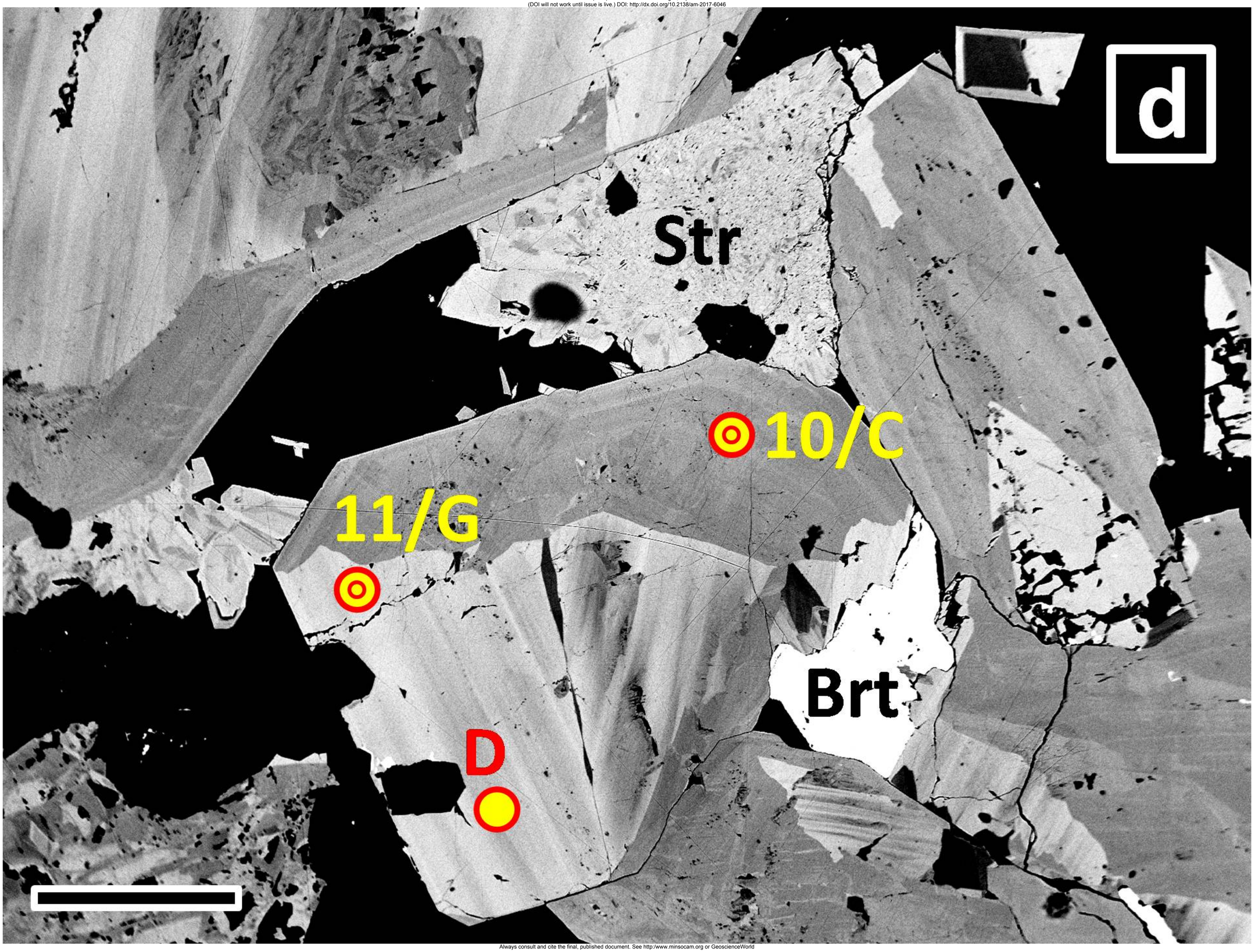

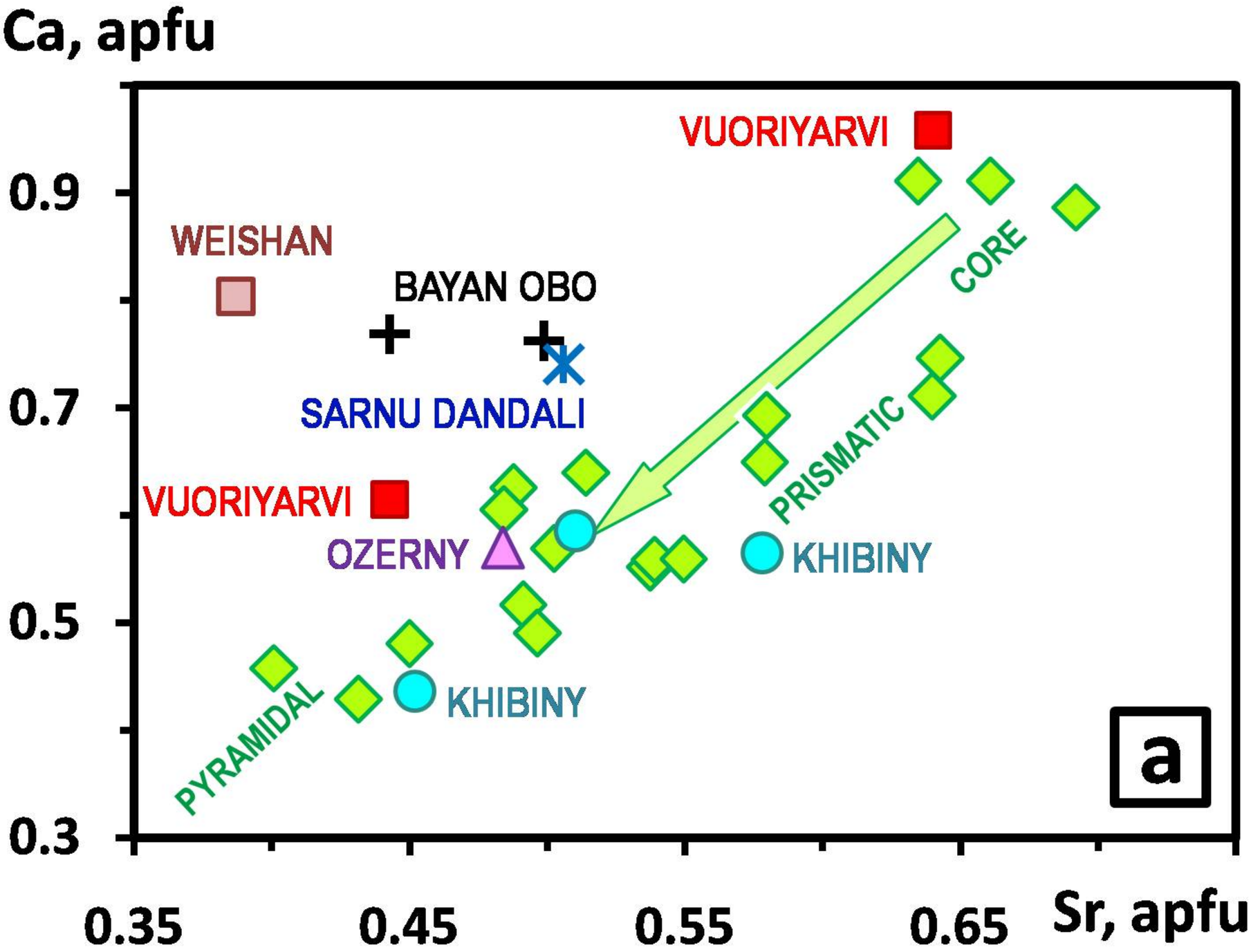

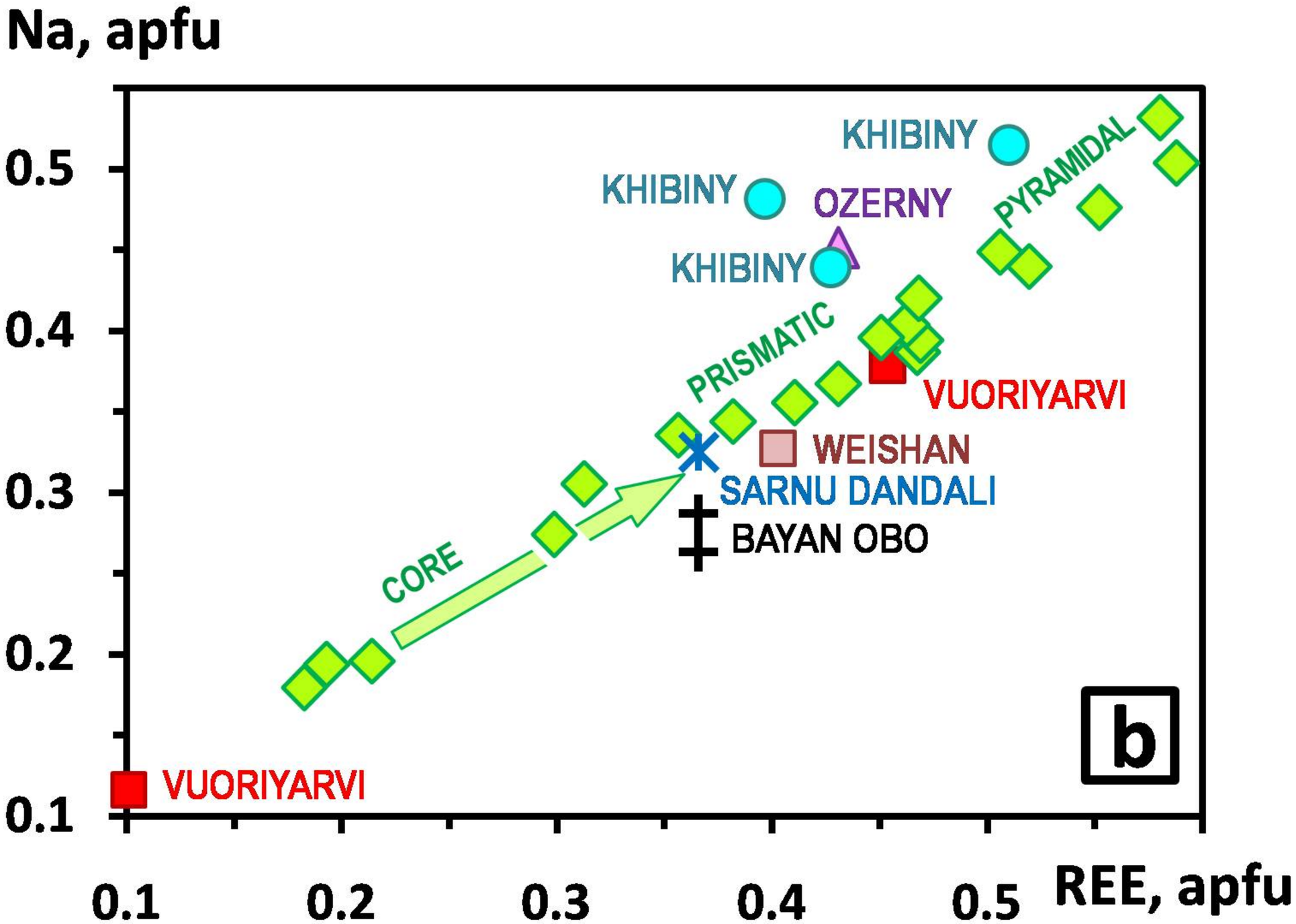

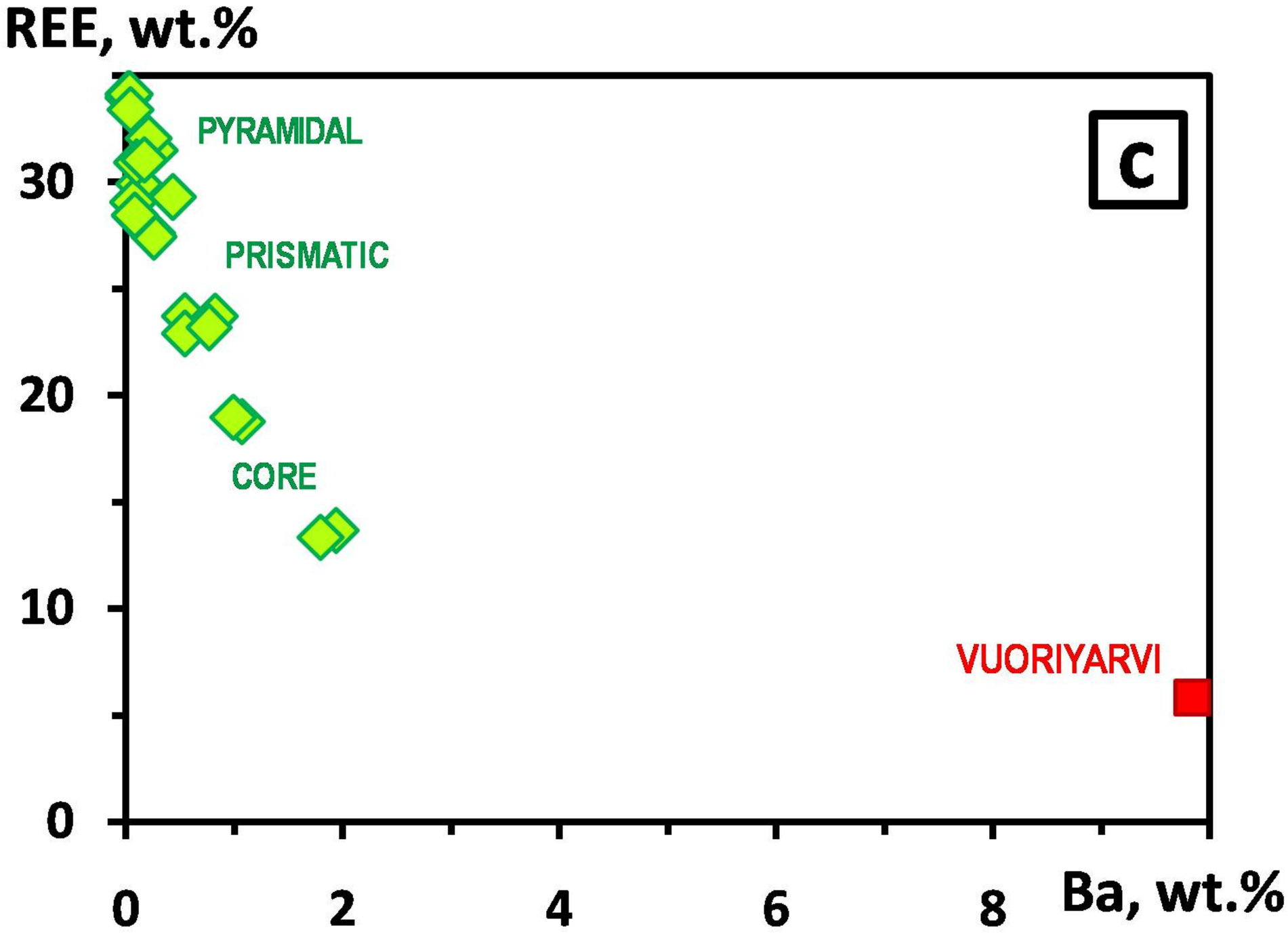

This is a preprint, the final version is subject to change, of the American Mineralogist (MSA)
Cite as Authors (Year) Title. American Mineralogist, in press.
(DOI will not work until issue is live.) DOI: http://dx.doi.org/10.2138/am-2017-6046

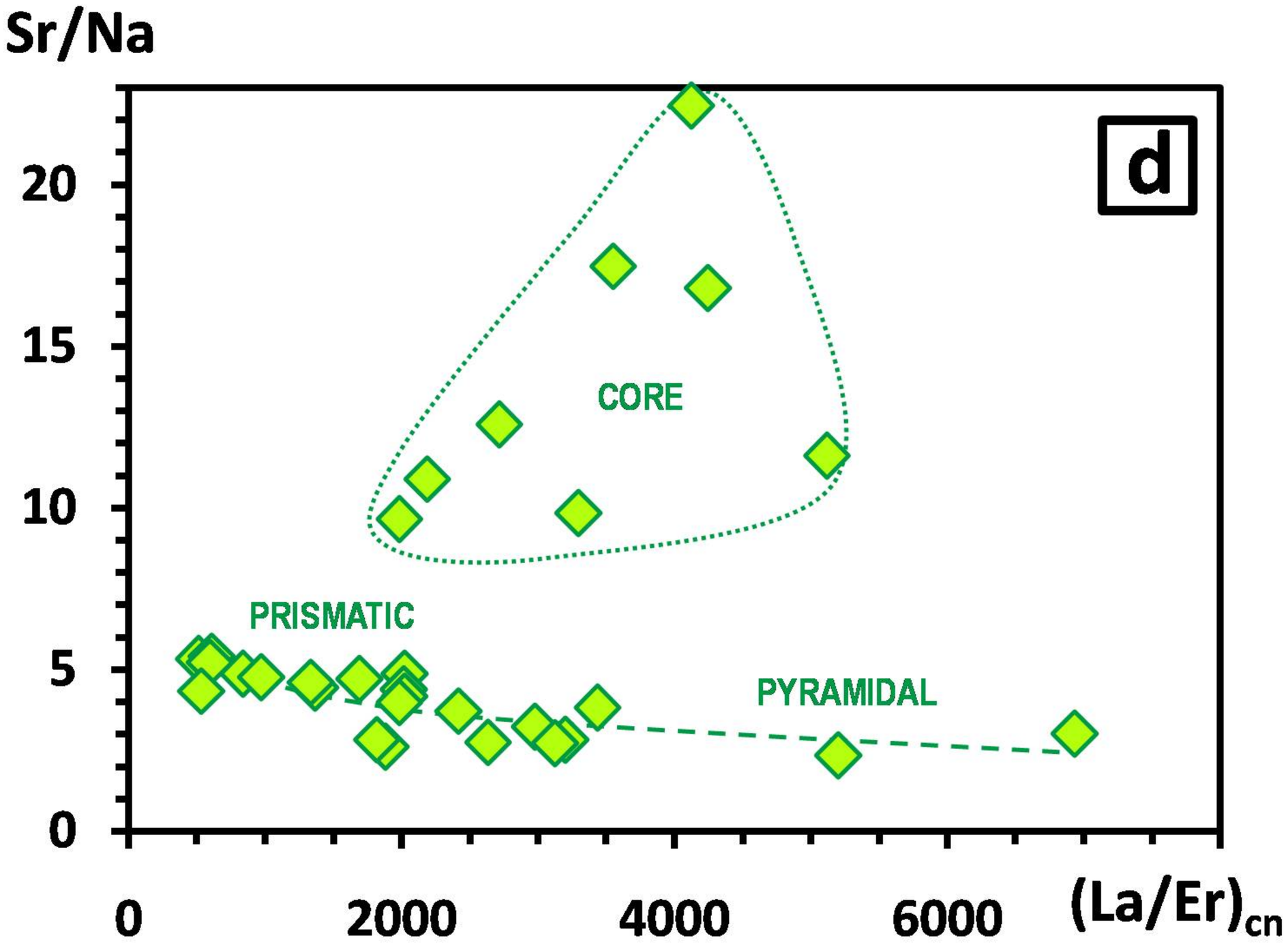

This is a preprint, the final version is subject to change, of the American Mineralogist (MSA)
Cite as Authors (Year) Title. American Mineralogist, in press.
(DOI will not work until issue is live.) DOI: http://dx.doi.org/10.2138/am-2017-6046

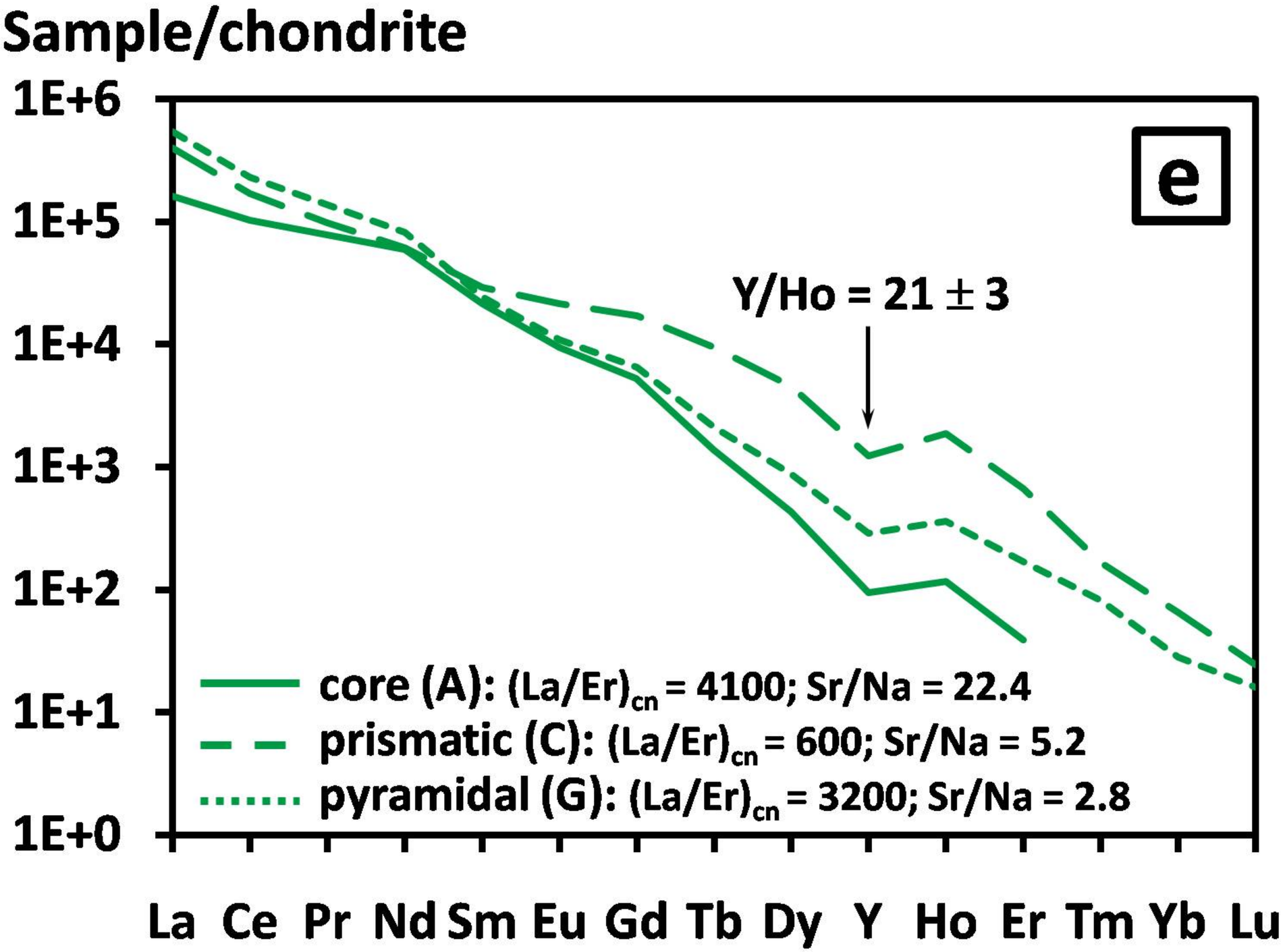

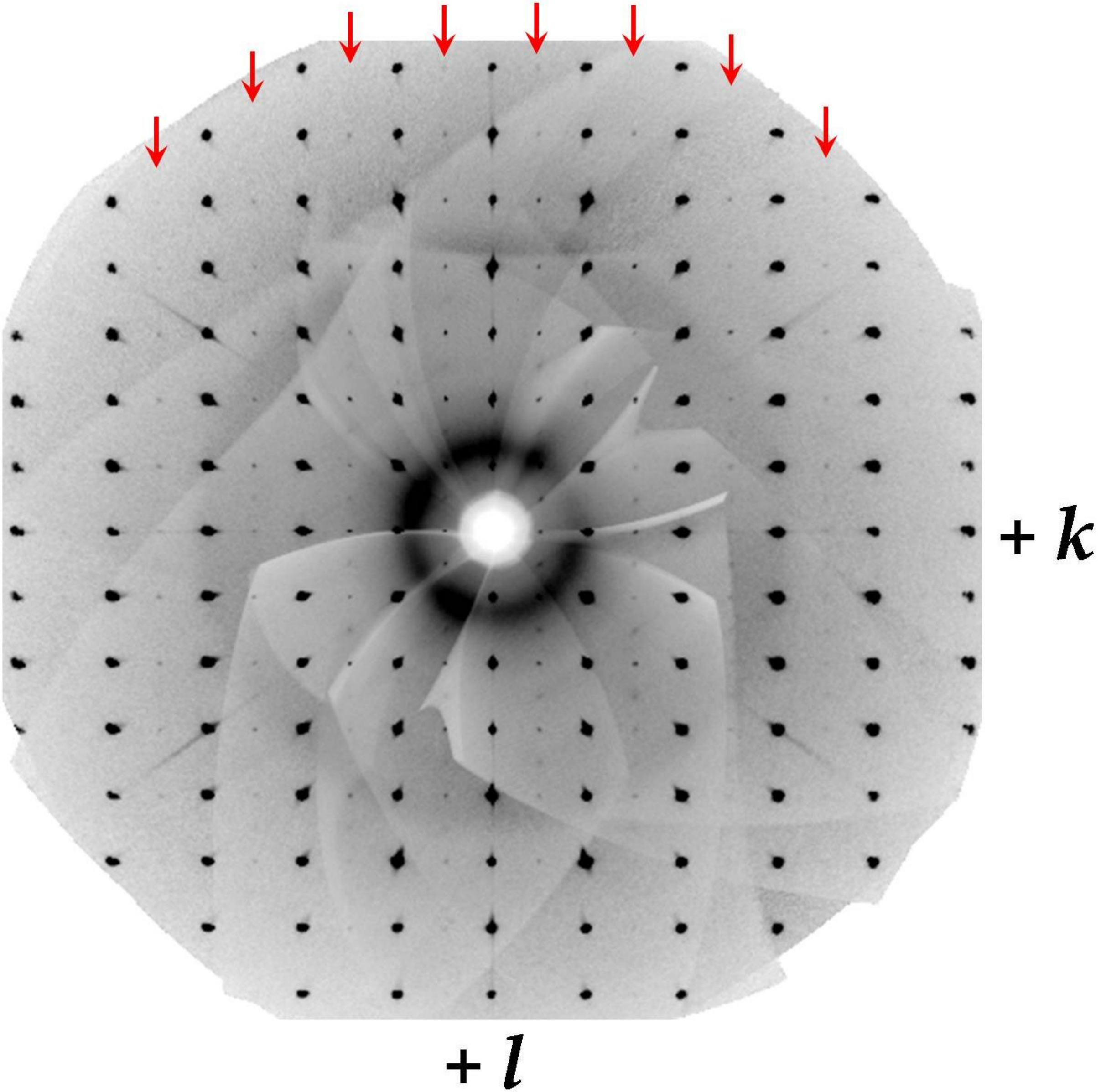

This is a preprint, the final version is subject to change, of the American Mineralogist (MSA)
Cite as Authors (Year) Title. American Mineralogist, in press.
(DOI will not work until issue is live.) DOI: http://dx.doi.org/10.2138/am-2017-6046

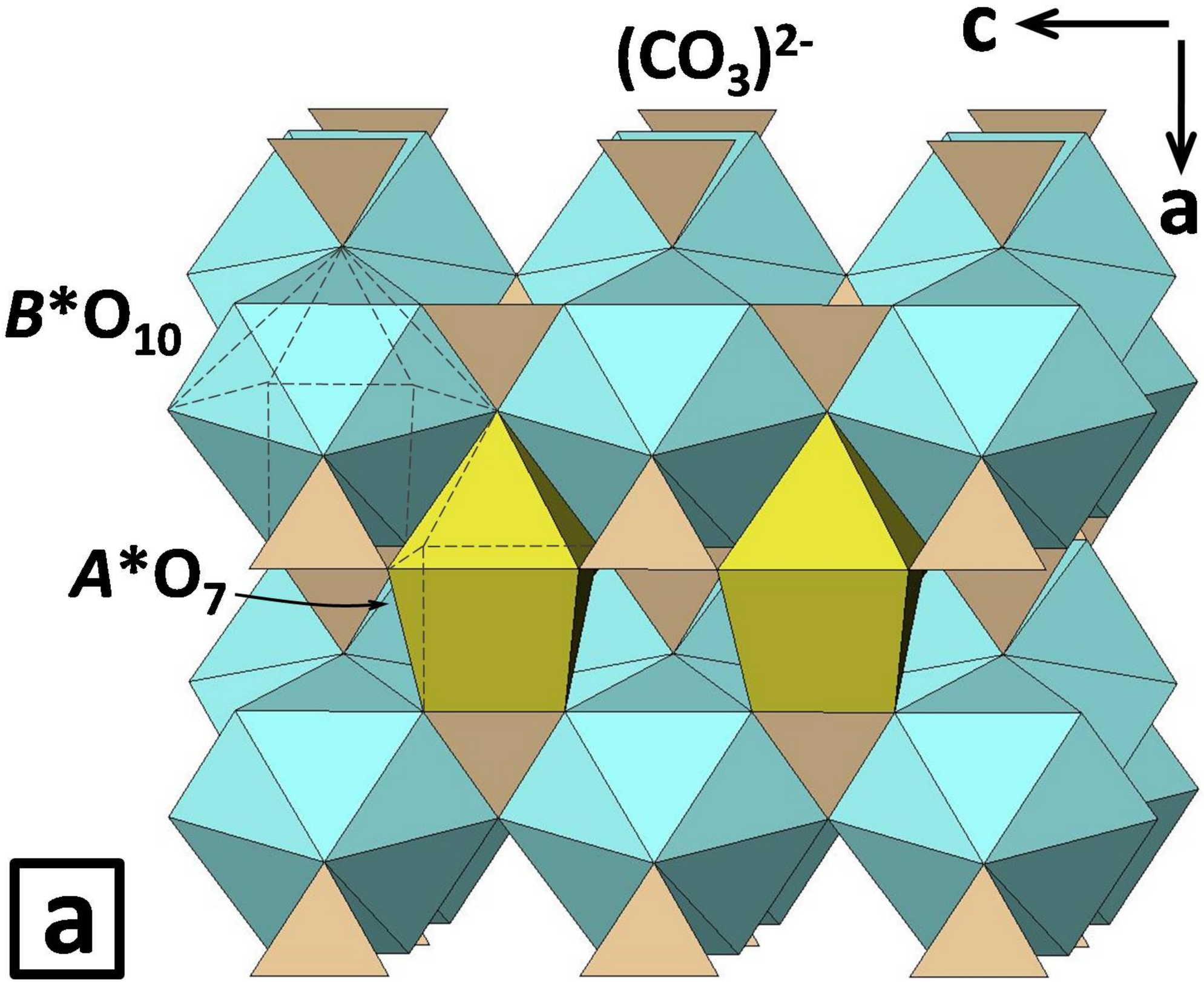

This is a preprint, the final version is subject to change, of the American Mineralogist (MSA)
Cite as Authors (Year) Title. American Mineralogist, in press.
(DOI will not work until issue is live.) DOI: http://dx.doi.org/10.2138/am-2017-6046

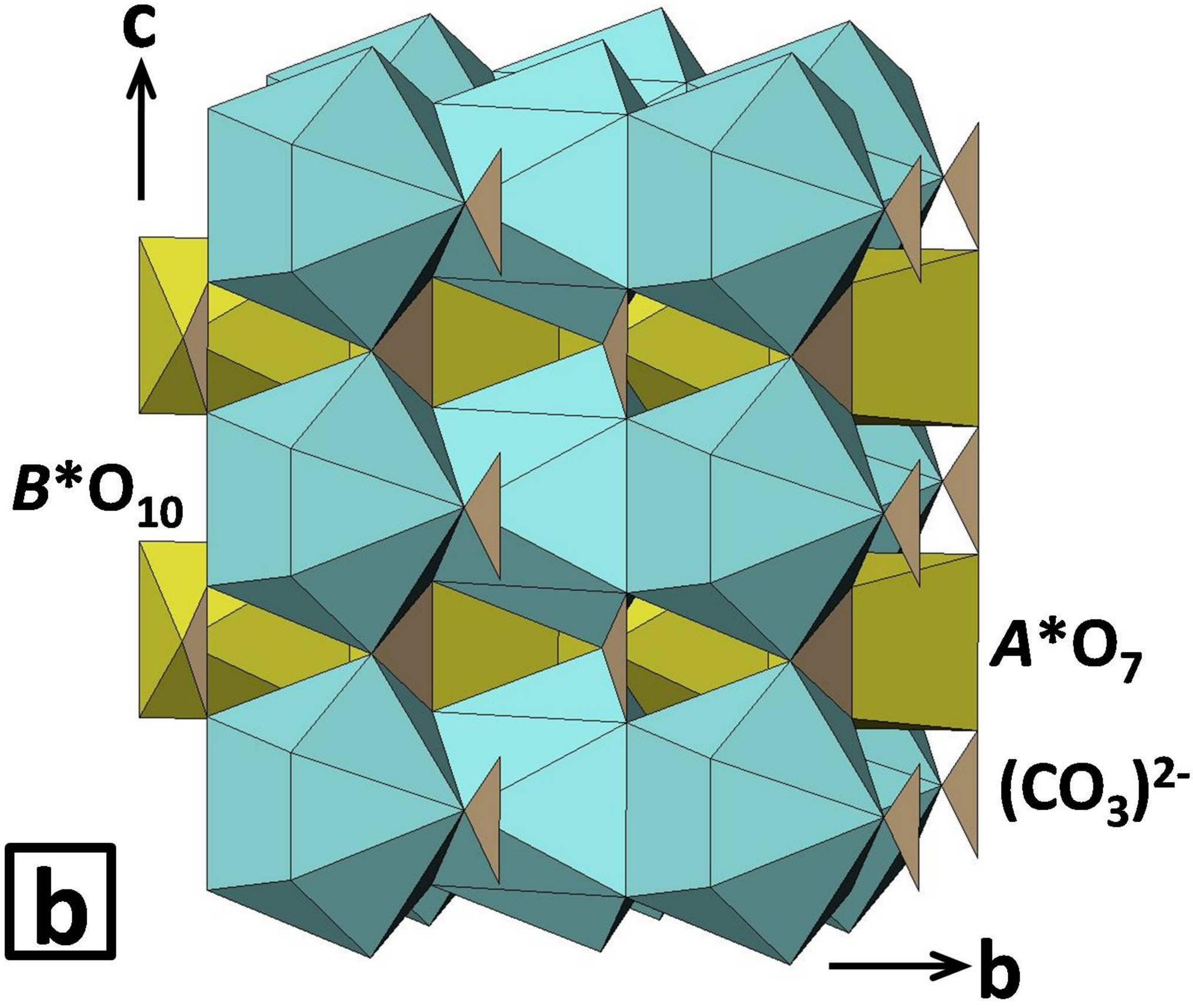

This is a preprint, the final version is subject to change, of the American Mineralogist (MSA)
Cite as Authors (Year) Title. American Mineralogist, in press.
(DOI will not work until issue is live.) DOI: http://dx.doi.org/10.2138/am-2017-6046

CARBOCERNAITE

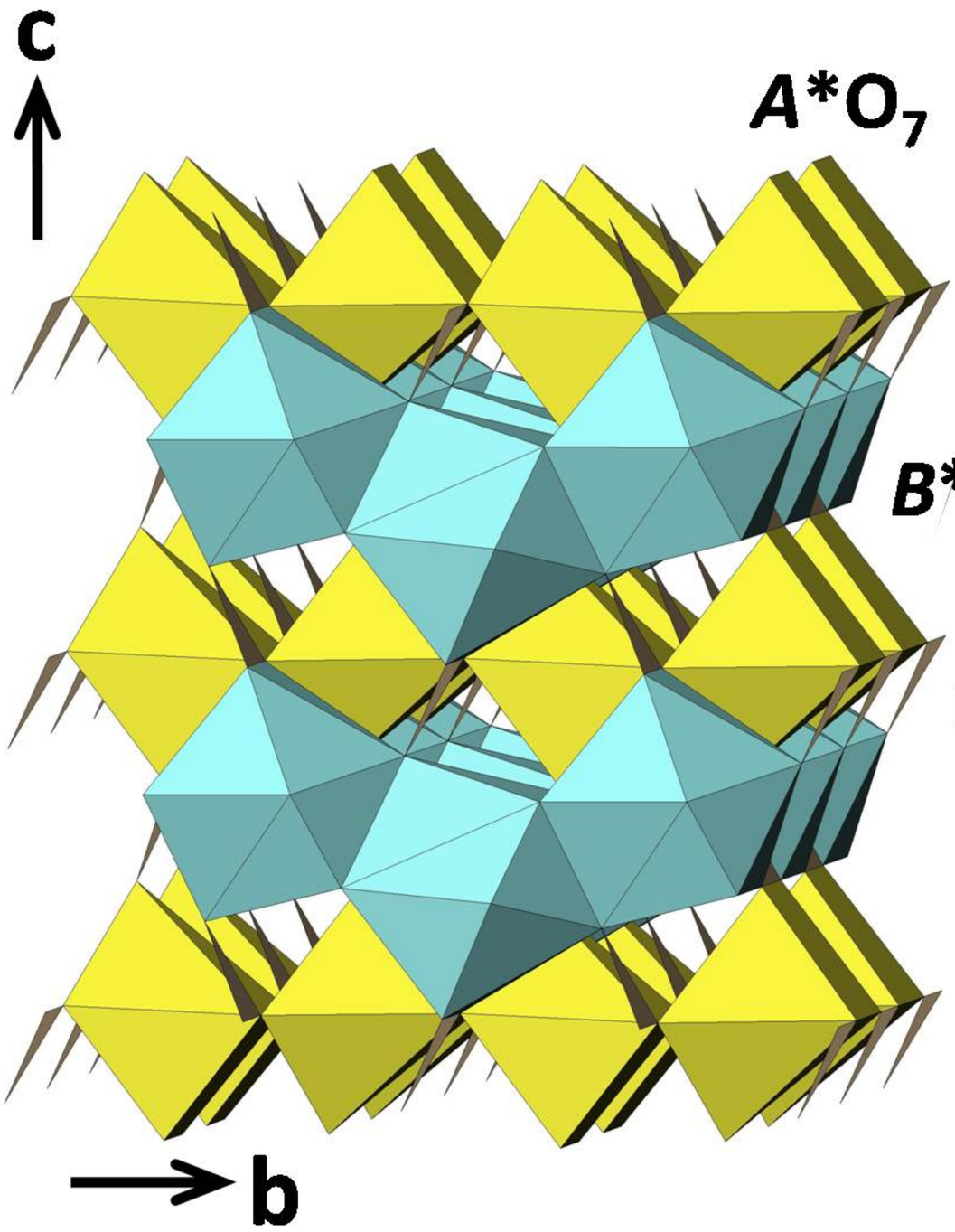

BARYTOCALCITE

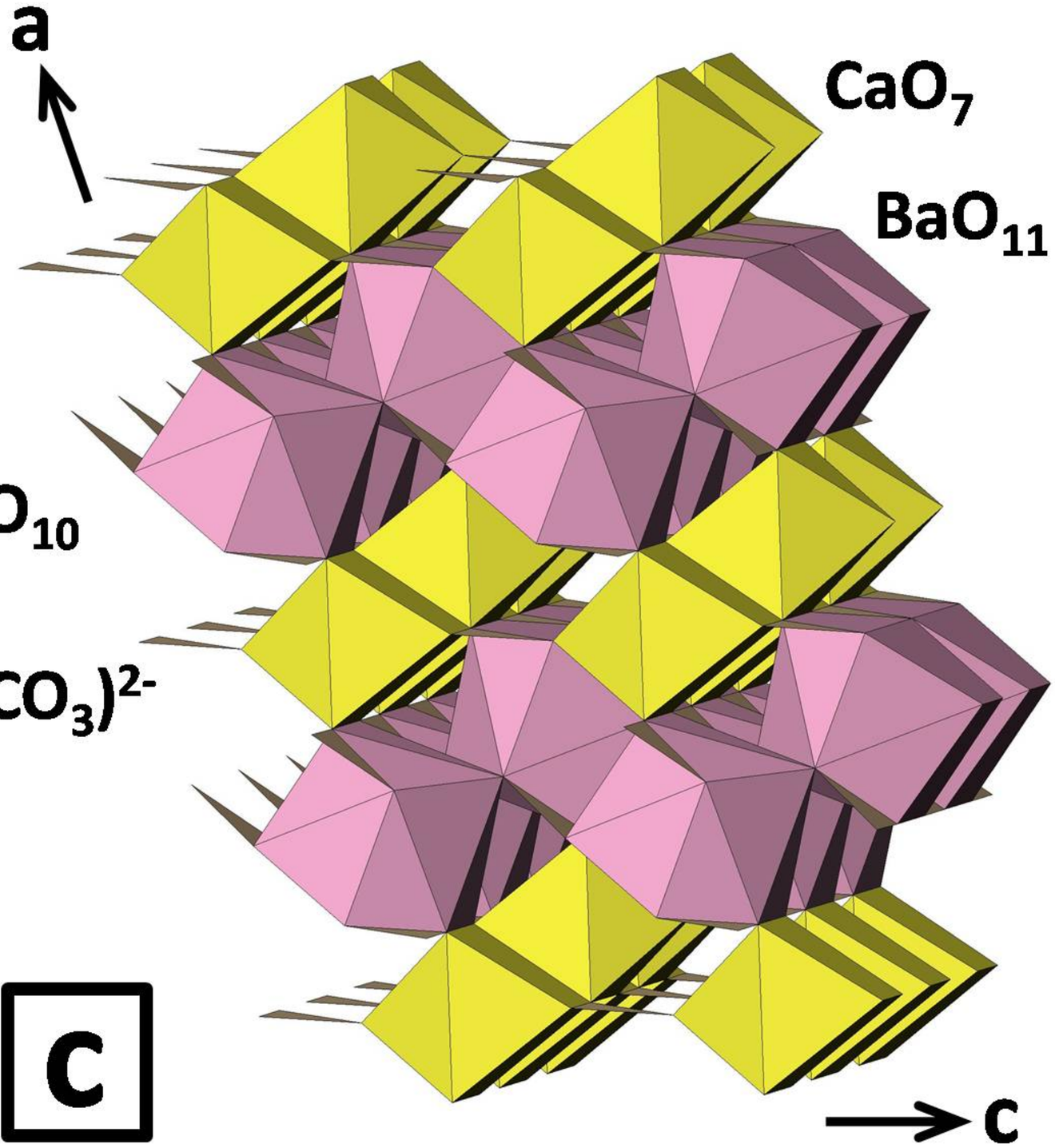

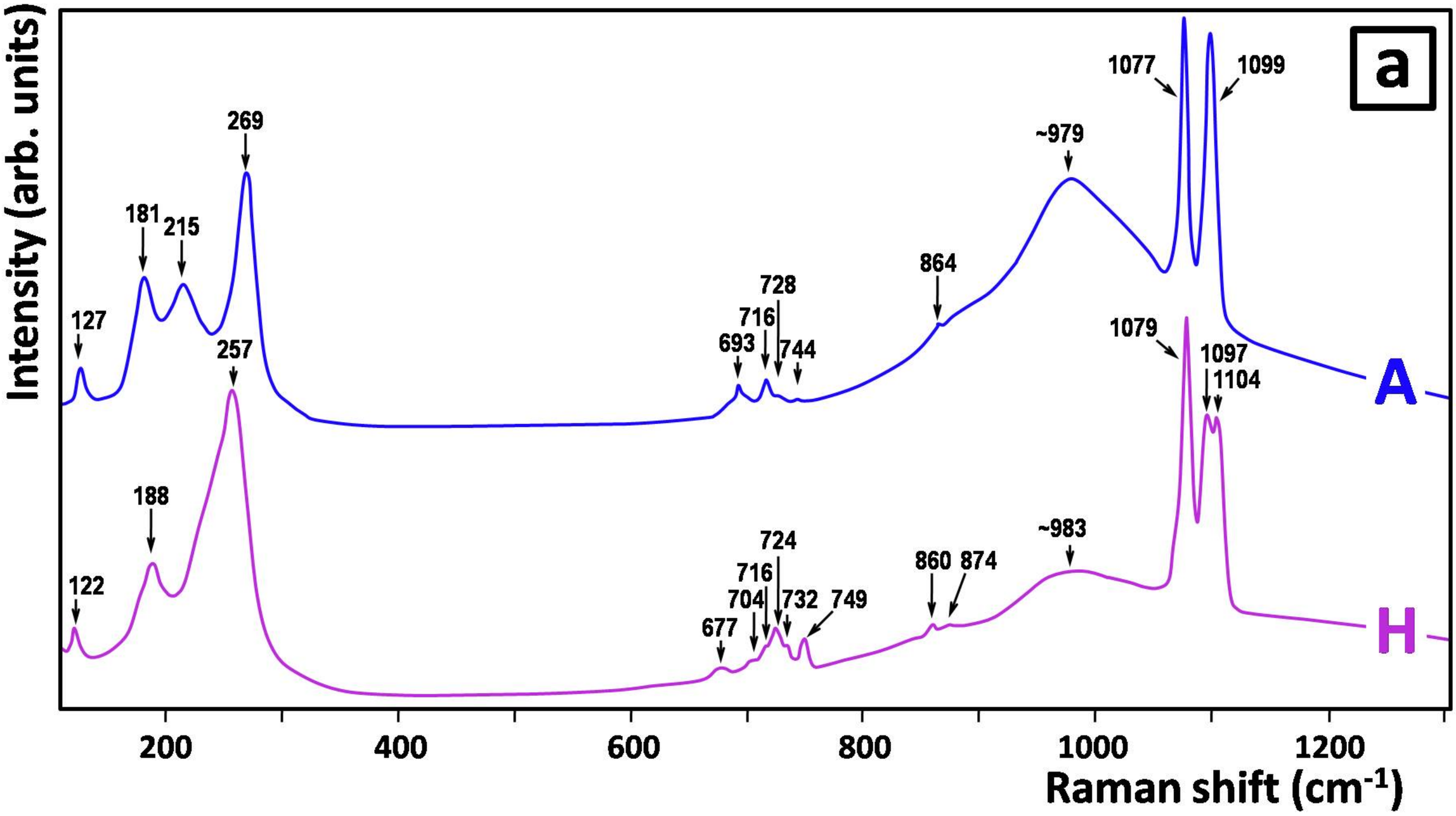

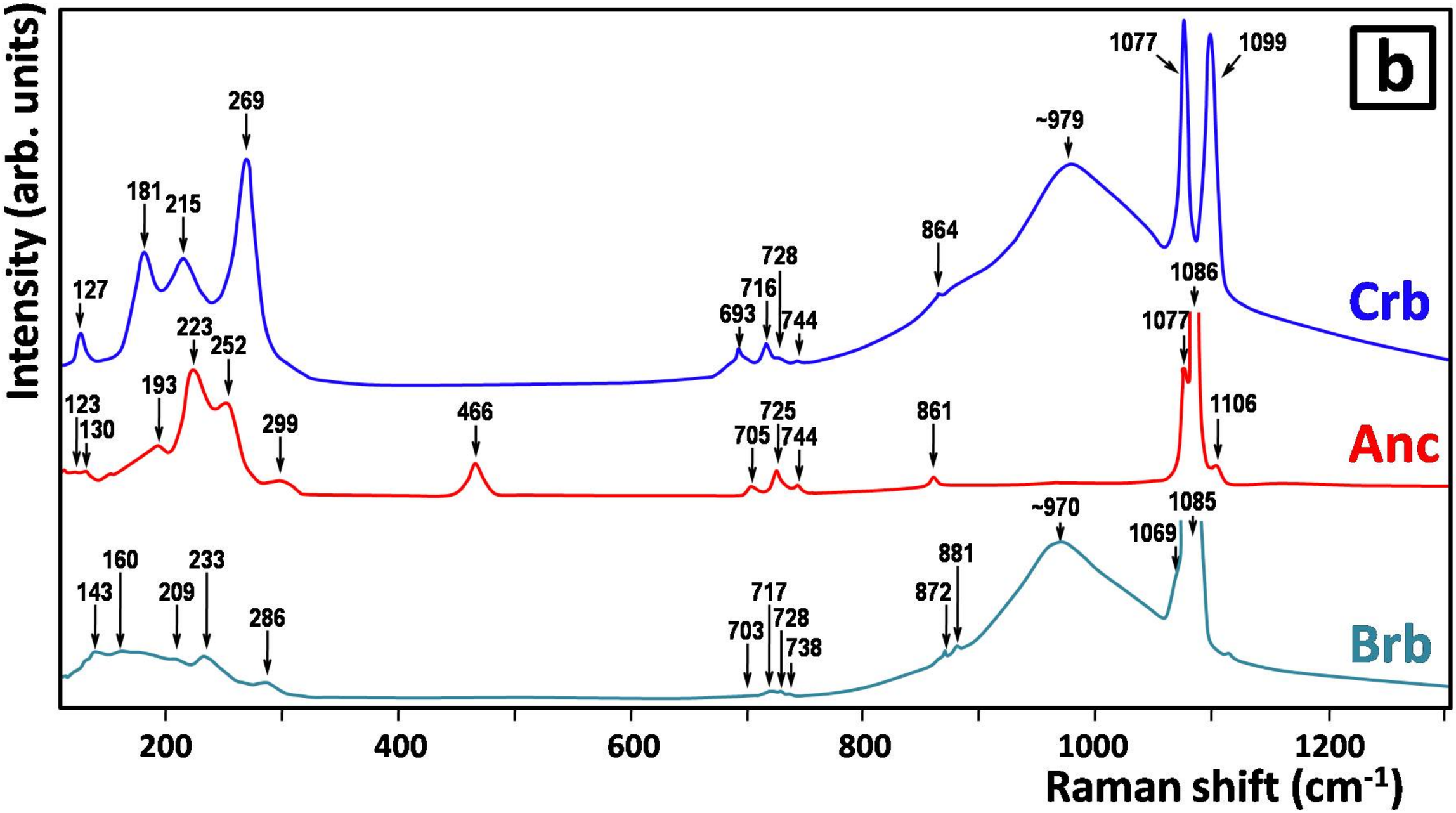

This is a preprint, the final version is subject to change, of the American Mineralogist (MSA)
Cite as Authors (Year) Title. American Mineralogist, in press.
(DOI will not work until issue is live.) DOI: http://dx.doi.org/10.2138/am-2017-6046

Pseudomorphs with Cer and major Anc

Ce-depleted, ^{18}O-rich $(SO_4)^{2-}$ fluids

Pseud. with major Anc, Brt (± Mnz), no Crb

Py oxidation

◁ Redox front

Pseudomorphs with Crb, minor Anc, Brt

$(SO_4)^{2-}$ reduction; Mrc ⇒ Py

Brb resorption by fluids

Primary Brb

This is a preprint, the final version is subject to change, of the American Mineralogist (MSA)
Cite as Authors (Year) Title. American Mineralogist, in press.
(DOI will not work until issue is live.) DOI: http://dx.doi.org/10.2138/am-2017-6046

TABLE 1. Geochemical characteristics of the carbocernaite-bearing carbonatite sample from Bear Lodge, Wyoming

Drill hole no. RES08-4 Sampling depth 459.2 m

Whole-rock major- and trace-element abundances[a]:

	wt.%		ppm		ppm
SiO_2	0.49	Rb	2.8	Sc	4
TiO_2	< 0.01	Ba	6734	Y	413.0
Al_2O_3	0.13	Pb	668.5	La	10335.1
MgO	0.16	Co	8.2	Ce	18712.8
CaO	24.31	Ni	1.5	Pr	1849.5
MnO	2.01	Zn	1455	Nd	7778.9
FeO[b]	0.19	Cd	13.4	Sm	1285.6
Fe[c]	14.80	V	27	Eu	291.0
SrO	> 5.00	Ga	5.9	Gd	680.8
Na_2O	0.70	Bi	67	Tb	54.6
K_2O	0.06	As	47	Dy	170.6
P_2O_5	0.11	Se	21.8	Ho	13.1
CO_2	26.51	Zr	7.0	Er	20.0
S[d]	17.13	Th	389.1	Tm	2.4
F	0.04	U	1.5	Yb	15.9
		Nb	7.0	Lu	1.7

Selected trace-element and isotopic ratios:

Whole-rock:		Magmatic calcite (Cal1 in Fig. 1):	
Ga/Al	0.0086	$(La/Yb)_{cn}$	0.1-1.1
$(La/Yb)_{cn}$	450	Y/Ho	24.9-29.5
Y/Ho	31.5	δCe	0.9-1.0
Th/U	259	δEu	1.0-1.2
$(^{87}Sr/^{86}Sr)_I$	0.704620[e]	$\delta^{13}C_{V\text{-}PDB}$, ‰	–7.0[e]
$(^{143}Nd/^{144}Nd)_I$	0.512605[e]	$\delta^{18}O_{V\text{-}SMOW}$, ‰	10.9[e]
Magmatic burbankite[f]:		Hydrothermal calcite (Cal2):	
δCe	1.1	$\delta^{13}C_{V\text{-}PDB}$, ‰	–6.7[e]
Magmatic fluorapatite[f]:		$\delta^{18}O_{V\text{-}SMOW}$, ‰	18.0[e]
δCe	1.0	Hydrothermal pyrite:	
		$\delta^{34}S_{V\text{-}CDT}$, ‰	–9.35[g]

[a] Analyzed at Acme Labs (Vancouver, Canada) by a combination of X-ray fluorescence, inductively-coupled-plasma mass-spectrometry, and combustion infrared techniques; Cs, Hf and Ta are < 0.1 ppm; Be and Sn are < 1 ppm.

[b] Total Fe after subtraction of Fe in pyrite, expressed as FeO.

[c] Fe in pyrite.

[d] Total S, including an estimated ~17.0% S in sulfides and ~0.4% SO_3 in barite.

[e] For details of isotopic measurements, see Moore et al. (2015).

[f] Eu, Y and Ho data are not available for these minerals.

[g] Average of two measurements (–9.5 and –9.2‰) obtained at the Stable Isotope Laboratory (University of Manitoba) with a relative precision of 0.3‰.

This is a preprint, the final version is subject to change, of the American Mineralogist (MSA)
Cite as Authors (Year) Title. American Mineralogist, in press.
(DOI will not work until issue is live.) DOI: http://dx.doi.org/10.2138/am-2017-6046

TABLE 2. Representative WDS analyses of carbocernaite from Bear Lodge

Spot no.[a]	1	2	3	4	5[b]	6	7	8	9	10	11
wt.%											
Na_2O	2.23	4.19	3.56	4.69	4.86	5.19	6.05	2.39	3.25	4.13	5.36
CaO	20.49	13.35	15.00	12.04	11.92	10.82	8.84	19.81	16.00	14.11	9.79
SrO	27.46	19.23	24.95	21.45	19.45	19.01	16.43	28.56	25.47	23.23	16.94
BaO	3.95	0.86	1.36	0.09	0.77	0.49	b.d.	2.13	1.46	1.08	0.19
Y_2O_3	b.d.[b]	b.d.	b.d.	b.d.	b.d.	b.d.	b.d.	b.d.	b.d.	0.14	b.d.
La_2O_3	3.49	9.20	5.84	10.69	8.94	11.48	10.77	4.69	6.42	9.47	12.64
Ce_2O_3	5.75	12.27	9.16	15.44	14.34	15.40	18.39	6.11	9.34	11.99	16.35
Pr_2O_3	0.69	1.28	1.03	1.34	1.40	1.34	1.74	0.62	0.76	1.04	1.35
Nd_2O_3	1.66	2.35	2.53	2.09	3.49	2.57	4.05	1.02	1.75	1.28	2.25
Sm_2O_3	0.47	0.57	0.84	b.d.	0.61	0.23	0.09	0.18	0.52	0.50	0.31
ThO_2	b.d.	0.56	0.17	b.d.	0.14	b.d.	0.14	b.d.	0.07	0.17	b.d.
CO_2[c]	35.29	32.36	33.12	33.81	32.88	32.87	32.34	35.06	33.66	34.09	31.98
Total	101.48	96.22	97.56	101.64	98.79	99.40	98.84	100.57	98.70	101.23	97.16
Formulae calculated on the basis of six atoms of oxygen (two carbonate groups):											
Na	0.179	0.368	0.305	0.394	0.420	0.448	0.531	0.194	0.274	0.344	0.476
Ca	0.911	0.647	0.711	0.559	0.569	0.517	0.429	0.887	0.746	0.650	0.480
Sr	0.661	0.505	0.640	0.539	0.502	0.491	0.432	0.692	0.643	0.579	0.450
Ba	0.064	0.015	0.024	0.002	0.013	0.009	-	0.035	0.025	0.018	0.003
Y	-	-	-	-	-	-	-	-	-	0.003	-
La	0.053	0.154	0.095	0.171	0.147	0.189	0.180	0.072	0.103	0.150	0.214
Ce	0.087	0.203	0.148	0.245	0.234	0.251	0.305	0.093	0.149	0.189	0.274
Pr	0.010	0.021	0.017	0.021	0.023	0.022	0.029	0.009	0.012	0.016	0.023
Nd	0.025	0.038	0.040	0.032	0.056	0.041	0.066	0.015	0.027	0.020	0.037
Sm	0.007	0.009	0.013	-	0.009	0.004	0.001	0.003	0.008	0.007	0.005
Th	-	0.006	0.002	-	0.001	-	0.001	-	0.001	0.002	-
Σcations	1.997	1.966	1.995	1.963	1.974	1.972	1.974	2.000	1.988	1.978	1.962

[a] See Figure 2 for the location of WDS analyses.
[b] Material examined by single-crystal X-ray diffraction.
[c] b.d. = below detection by WDS.
[d] CO_2 calculated on the basis of stoichiometry.

This is a preprint, the final version is subject to change, of the American Mineralogist (MSA)
Cite as Authors (Year) Title. American Mineralogist, in press.
(DOI will not work until issue is live.) DOI: http://dx.doi.org/10.2138/am-2017-6046

TABLE 3. Representative LA-ICP-MS spot analyses of carbocernaite from Bear Lodge[a]

ppm	A	B	C	D	E	F	G	H	I
Mn	52	57	165	76	283	58	84	80	88
Y	147	350	1923	468	741	471	450	407	767
Ba	19398	10731	8248	2592	833	4396	2180	460	212
La	37869	60001	93056	80405	100593	104238	127796	109743	115162
Ce	61464	84258	102331	125533	131801	131475	139616	156956	156956
Pr	6906	8607	8676	13961	11593	12150	12245	14868	15268
Nd	26891	29072	27764	48957	35832	39528	37061	47606	48350
Sm	3182	4890	4283	4862	3678	4831	3578	4443	4724
Eu	527	1053	1204	758	765	887	615	686	821
Gd	1045	2332	3353	1301	1785	1710	1272	1303	1623
Tb	50	125	339	65	151	97	76	71	98
Dy	104	254	1093	185	447	247	213	179	292
Ho	6	18	104	18	43	21	20	17	31
Er	6	12	106	27	40	29	27	24	41
Tm	< 0.3	0.6	4.0	1.8	1.6	1.6	2.0	1.4	2.5
Yb	< 1.8	< 1.3	10.6	6.7	4.0	6.0	4.6	6.8	7.1
Lu	< 0.4	< 0.4	0.6	0.6	< 0.4	< 0.4	0.4	0.4	0.5
Pb	5.4	4.4	10.5	5.2	8.7	3.0	4.3	7.0	8.7
Th	866	581	1946	855	1405	590	730	1312	1697
U	< 0.8	< 0.6	0.8	< 0.5	< 0.6	0.6	0.5	< 0.6	0.5
Sr/Na[b]	22.4	9.8	5.2	4.4	4.7	3.7	2.8	2.7	2.6
Sr/Ba[b]	23	24	23	75	244	38	66	299	667
$(La/Er)_{cn}$[c]	4122	3300	597	2019	1693	2420	3202	3125	1883
Y/Ho	23	19	19	25	17	23	22	24	25
δCe	0.85	0.79	0.69	0.83	0.78	0.75	0.68	0.82	0.79
δEu	0.70	0.83	0.93	0.68	0.80	0.76	0.71	0.67	0.73

[a] See Figure 2 for the location of analyzed areas.
[b] Calculated from the Sr values determined by WDS.
[c] Chondrite normalization (cn) values are from Anders and Grevesse (1989).

This is a preprint, the final version is subject to change, of the American Mineralogist (MSA)
Cite as Authors (Year) Title. American Mineralogist, in press.
(DOI will not work until issue is live.) DOI: http://dx.doi.org/10.2138/am-2017-6046

TABLE 4. Miscellaneous crystallographic information for carbocernaite

a (Å)	6.434(4)	Crystal size (μm)	40 × 80 × 80
b (Å)	7.266(5)	Radiation	Mo*K*α
c (Å)	5.220(3)	No. of reflections	9331
γ (°)	89.979(17)	No. in Ewald sphere	2870
V (Å^3)	244.0(5)	No. unique reflections	1588
Space group	*P*11*m*	No. with (*Fo* > 4σ*F*)	1577
Z	2	R_{merge}, %	1.0
Twin fraction	0.101(13)	R_1, %	1.6
Racemic fractions	0.208(13), 0.370(13)	wR_2, %	4.2

$R_1 = \Sigma(|Fo| - |Fc|) / \Sigma|Fo|$

$wR_2 = [\Sigma w(Fo^2 - Fc^2)^2 / \Sigma w(Fo^2)^2]^{½}$, $w = 1 / [\sigma^2(Fo^2) + (0.0236\ P)^2 + 0.36\ P]$, where $P = (\max(Fo^2, 0) + 2Fc^2) / 3$

TABLE 5. Atom coordinates and anisotropic-displacement parameters (Å^2) for carbocernaite

Site	*x*	*y*	*z*	U_{11}	U_{22}	U_{33}	U_{23}	U_{13}	U_{12}	U_{eq}
A	0.0269(4)	0.7016(5)	½	0.0167(8)	0.0156(9)	0.0149(8)	0	0	-0.0012(6)	0.0157(7)
A'	-0.0135(4)	0.2015(5)	½	0.0190(8)	0.0160(9)	0.0145(7)	0	0	0.0012(6)	0.0165(6)
B	0.38015(7)	0.0000(3)	0	0.0164(2)	0.0135(3)	0.01275(19)	0	0	-0.0034(4)	0.01421(16)
B'	-0.37917(5)	0.49934(18)	0	0.00681(14)	0.0115(2)	0.01035(14)	0	0	-0.0019(4)	0.00954(11)
*C*1	0.0884(13)	0.4113(11)	0	0.0109(15)	0.0099(14)	0.0111(14)	0	0	-0.0015(9)	0.0106(12)
*C*1'	-0.0812(16)	0.9178(13)	0	0.0146(15)	0.0131(16)	0.0142(15)	0	0	0.0006(9)	0.0140(13)
*C*2	0.4712(18)	0.6734(16)	½	0.0165(16)	0.0158(17)	0.0160(17)	0	0	0.0004(9)	0.0161(15)
*C*2'	-0.4641(16)	0.1730(13)	½	0.0120(14)	0.0108(15)	0.0106(15)	0	0	0.0002(9)	0.0111(13)
O1	0.3762(15)	0.7055(5)	0.2844(8)	0.0151(10)	0.0190(10)	0.0153(10)	0.0003(8)	-0.0011(8)	0.0009(8)	0.0164(7)
O1'	-0.3705(18)	0.2044(5)	0.2864(8)	0.0193(12)	0.0209(10)	0.0168(10)	0.0008(8)	0.0015(9)	-0.0007(9)	0.0190(8)
O2	0.0075(8)	0.9553(4)	0.2099(7)	0.0189(11)	0.0194(11)	0.0157(10)	-0.0015(8)	-0.0018(8)	0.0016(8)	0.0180(8)
O2'	-0.0093(9)	0.4544(4)	0.2106(6)	0.0185(10)	0.0193(11)	0.0131(10)	-0.0014(7)	0.0019(8)	-0.0008(8)	0.0170(7)
O3	0.3494(14)	0.1062(8)	½	0.0215(14)	0.0245(15)	0.0222(14)	0	0	-0.0032(9)	0.0227(12)
O3'	-0.3538(13)	0.5976(8)	½	0.0235(15)	0.0271(15)	0.0239(14)	0	0	0.0035(9)	0.0249(13)
O4	0.2624(12)	0.3329(8)	0	0.0208(14)	0.0221(14)	0.0247(14)	0	0	0.0035(9)	0.0225(12)
O4'	-0.2611(12)	0.8328(8)	0	0.0207(14)	0.0224(13)	0.0250(14)	0	0	-0.0040(9)	0.0227(11)

This is a preprint, the final version is subject to change, of the American Mineralogist (MSA)
Cite as Authors (Year) Title. American Mineralogist, in press.
(DOI will not work until issue is live.) DOI: http://dx.doi.org/10.2138/am-2017-6046

TABLE 6. Fractional coordinate difference between pseudosymmetric site pairings in carbocernaite

Site pair	Δ *x* / <σ>*	Δ *y* / <σ>*	Δ *z* / <σ>*
A – *A*'	34	0	–
B – *B*'	16	3	–
*C*1 – *C*1'	5	5	–
*C*2 – *C*2'	4	0	–
O1 – O1'	3	2	3
O2 – O2'	2	2	1
O3 – O3'	3	11	–
O4 – O4'	1	0	–

* Δ *x* / <σ> = |*x* - *x*'| / <σ> ; Δ *y* / <σ> = |(|*y* - *y*'| - 0.5)| / <σ> ; Δ *z* / <σ> = |*z* - *z*'| / <σ>

TABLE 7. Selected interatomic distances (Å) in carbocernaite

A – O1	2.513(9) × 2	*A*' – O1'	2.553(11) × 2
A – O2	2.389(4) × 2	*A*' – O2'	2.379(4) × 2
A – O2'	2.359(4) × 2	*A*' – O2	2.347(4) × 2
A – O3'	2.564(9)	*A*' – O3	2.435(10)
<*A* – O>	2.441	<*A*' – O>	2.428
B – O1	2.604(4) × 2	*B*' – O1'	2.613(4) × 2
B – O1'	2.649(8) × 2	*B*' – O1	2.631(7) × 2
B – O2	2.657(5) × 2	*B*' – O2'	2.642(6) × 2
B – O3	2.729(2) × 2	*B*' – O3'	2.711(2) × 2
B – O4	2.534(7)	*B*' – O4'	2.540(7)
B – O4'	2.608(8)	*B*' – O4	2.604(7)
<*B* – O>	2.642	<*B*' – O>	2.634
*C*1 – O2'	1.304(5) × 2	*C*1' – O2	1.265(5) × 2
*C*1 – O4	1.256(10)	*C*1' – O4'	1.312(11)
<*C*1 – O>	1.288	<*C*1' – O>	1.281
*C*2 – O1	1.302(8) × 2	*C*2' – O1'	1.288(8) × 2
*C*2 – O3'	1.253(14)	*C*2' – O3	1.295(12)
<*C*2 – O>	1.286	<*C*2' – O>	1.290